NASA CONTRACTOR REPORT

NASA CR-2226

NASA CR-2226

DEVELOPMENT OF A HIGH SPEED PARALLEL HYBRID BOOST BEARING

by L. W. Winn and M. W. Eusepi

Prepared by
MECHANICAL TECHNOLOGY INCORPORATED
Latham, N.Y. 12110
for Lewis Research Center

NATIONAL AERONAUTICS AND SPACE ADMINISTRATION • WASHINGTON, D. C. • MARCH 1973

1. Report No.	2. Government Accession No.	3. Recipient's Catalog No.
NASA CR-2226		

4. Title and Subtitle	5. Report Date
DEVELOPMENT OF A HIGH SPEED PARALLEL HYBRID BOOST BEARING	March 1973
	6. Performing Organization Code

7. Author(s)	8. Performing Organization Report No.
L. W. Winn and M. W. Eusepi	MTI 72TR25
	10. Work Unit No.

9. Performing Organization Name and Address	11. Contract or Grant No.
Mechanical Technology Incorporated 968 Albany-Shaker Road Latham, New York 12110	NAS 3-14399
	13. Type of Report and Period Covered
12. Sponsoring Agency Name and Address	Contractor Report
National Aeronautics and Space Administration Washington, D.C. 20546	14. Sponsoring Agency Code

15. Supplementary Notes

Project Manager, William J. Anderson, Fluid System Components Division, NASA Lewis Research Center, Cleveland, Ohio

16. Abstract

The analysis, design, and testing of the hybrid boost bearing are discussed in this report. The hybrid boost bearing consists of a fluid film bearing coupled in parallel with a rolling element bearing. This coupling arrangement makes use of the inherent advantages of both the fluid film and rolling element bearing and at the same time minimizes their disadvantages and limitations. This report includes the analytical optimization studies that lead to the final fluid film bearing design. The bearing consisted of a centrifugally-pressurized planar fluid film thrust bearing with oil feed through the shaft center. An analysis of the test ball bearing is also presented. The experimental determination of the hybrid bearing characteristics obtained on the basis of individual bearing component tests and a combined hybrid bearing assembly is discussed and compared to the analytically determined performance characteristics.

17. Key Words (Suggested by Author(s))	18. Distribution Statement
Bearings Hybrid bearings Fluid film bearings Ball bearings	Unclassified - unlimited

19. Security Classif. (of this report)	20. Security Classif. (of this page)	21. No. of Pages	22. Price*
Unclassified	Unclassified	66	$3.00

* For sale by the National Technical Information Service, Springfield, Virginia 22151

TABLE OF CONTENTS

SUMMARY

The objective of this work was to develop a hybrid boost bearing applicable to advanced jet engine systems. The hybrid boost bearing configuration consists of a parallel combination of a planar fluid film bearing and a ball bearing. The fluid film bearing is unique in the sense that it takes advantage of centrifugal inertia forces established by rotor rotation to develop hydrostatic lubricant pressures. The pressurized lubricant is fed to a series of orifices which terminate in an annular groove at the bearing interface. The orifices are equally spaced, and the depth of the annular groove is designed so as to yield orifice compensation over the operating range of film thicknesses.

An analysis of the fluid film bearing combined with an optimization study for the specified conditions of operation was performed and coupled with an analysis of a 125 mm bore ball bearing. An existing test vehicle was modified to accommodate the new bearing design. The program terminated in a series of tests at rotor speeds which ranged between 10,000 and 20,000 rpm yielding a maximum DN value of 2.5 million, and axial loads ranging from 1,000 to 5,000 pounds. Testing was first performed on the ball bearing to establish its operational characteristics; this was followed by a series of fluid film bearing tests, and finally the fluid film bearing was combined with the ball bearing to form a hybrid boost bearing which was tested as a unit.

The test results indicate extremely good agreement between the analytical predictions and actual test data points for a speed of 10,000 rpm. The agreement between the analytical and test values on the rolling element bearing is still good at 15,000 rpm; however, the load carrying capacity of the fluid film bearing obtained at this speed falls short of the predicted values by a significant amount. The discrepancies at 20,000 rpm between the analytically-predicted and test values are high for both the fluid film and rolling element bearing. The differences in the rolling element bearing performance at the 20,000 rpm speeds can be attributed to high thermal gradients within the bearings causing a takeup in the bearing internal clearance.

The loss in load capacity experienced with the fluid film bearing at high speeds is attributed to film distortions caused by high thermal gradients across the bearing runner and stator. The effects of distortion appear to be further aggravated by the presence of high centrifugal pumping effects within the fluid film bearing oil film. All of these shortcomings can be corrected and the parallel hybrid boost bearing can be designed to provide a sound approach to the increase in the life of high-speed ball bearings.

INTRODUCTION

Continuous increases in design operating speeds, loads, and temperatures impose severe limitations on the reliability and life of rolling contact element bearings employed in advanced jet engine applications. One of the most critically stressed components is the main thrust bearing. The relatively brief life of that bearing (or set of bearings depending upon the design) influences to a very large extent the life of the overall system and its TBO. To accommodate the required thrust loads, these bearings are usually increased in size. This might be an acceptable solution as long as the speeds remain relatively low; at high speeds, however, a point in the bearing size is reached in which the centrifugal forces due to the orbital motion of the balls become the major limiting life factor.

The limitations affecting the performance of a rolling element bearing at high speeds have been recognized for many years. In order to provide solutions for these limitations, new and unique ideas have been generated. Many of these ideas focused on improved cleaner steels and the reduction in Hertzian stresses through improved conformity or compliance and through the employment of hollow or drilled balls. The cleaner steels have brought about an enormous improvement in the fatigue life of the ball bearing, thus stretching the range of its applicability to higher loads and higher speeds. The conforming and/or compliant bearing and the hollow ball concepts have been less successful and at present still remain in an early developmental stage [1-5]. In addition to the materials and compliant bearing studies, the rolling element bearing behavior has been analytically formulated thus permitting apriori optimization of bearing designs including any elastohydrodynamic phenomena occurring in the rolling contact bearing during operation [6,7].

The development of new high-temperature, light-weight engine structural materials along with advances made in the aerodynamic cycle performance has so far proceeded at a pace that in the near future will project engine capability beyond the advancements made in the bearings field; and the rolling element bearing may become the main limiting factor in further engine development.

The hybrid bearing concept provides a short cut towards the objective of supplying advanced engine designs with realistic long-life bearing arrangements. The hybrid bearing development programs in existence today cover series and parallel arrangements [8-12]. In the series arrangement, externally-imposed loads are carried equally by the fluid film and rolling element bearing, but the speed of the rolling element as well as the relative speed of the fluid film bearing are greatly reduced thus producing an increase in bearing life. In the parallel arrangement, herein referred to as the hybrid boost bearing, externally-applied loads acting on the ball bearing are reduced by virtue of load sharing between the fluid film and rolling element bearing while identical speed is maintained on both elements.

Hydrodynamic thrust bearings employed in the past at the relatively high speeds encountered in the fluid film bearing during operation with a hybrid boost bearing arrangment, have fallen short of developing the predicted load-carrying capacity [9,10]. The differences between the analytical predictions and the actual load-carrying capacities observed were partly due to the nonisothermal film behavior and to curvature effects within a thrust bearing which were not properly accounted for in the analytical treatment. One of the objectives of this program was to modify the existing analysis and to include temperature dependence, turbulence, and curvature effects. The results of this work are reported upon in Reference [13] covering the first analytical phase of this program.

Within the process of the fluid film bearing design for this particular program, it became apparent that a self-energized fluid film bearing which utilizes its own centrifugally-generated pressures to hydrostatically support load could offer substantial advantages in terms of power loss reduction and relative insensitivity to nonisothermal fluid film behavior. The hybrid boost bearing concept described in this report was thus built around the self-actuated orifice compensated fluid film thrust bearing. The rolling element bearing component consisted of a 125 mm bore split inner race ball bearing; this bearing was supplied by NASA-Lewis Engineering. A detailed discussion of the analytical, design, and test work performed on the hybrid boost bearing configuration is given in the following sections.

THE PARALLEL HYBRID BOOST BEARING DESIGN

The design of the parallel hybrid bearing involves the interrelation of a number of tasks. These tasks are categorized as follows:

- Design and optimization of the fluid film bearing to provide an acceptable load-deflection characteristic at a minimum power loss and lubricant flow rate requirement.
- Determination of the test ball bearing performance; primarily with regard to load-deflection characteristics.
- Combined ball bearing - fluid film bearing performance to assure adequate interaction between the two bearings when combined into the hybrid boost configuration.

Details of design for the parallel hybrid bearing are treated in the following report sections.

Fluid Film Bearing Design

Design of a fluid film bearing for application in jet engines must encompass two primary factors: flow and power loss. Ideally, a fluid film bearing designed for a jet engine application should require the least amount of flow possible. At the same time, the least amount of power should be dissipated since this represents a parasitic loss and imposes an additional burden on heat exchanger systems. The characteristics of a fluid film bearing are, however, generally such that the reduction in power loss is in many instances accompanied by an increase in flow; and, conversely, steps taken to decrease flow would have the tendency to increase power loss.

Because of the preponderance of different jet engine designs and sizes, a true "trade off" between flow and power loss cannot be generalized. Heat exchanger design and capacity, bearing sump design, bearing location, and materials are bound to heavily influence the weighting factors. As a result of the myriad of possible fluid film bearing design restrictions available, the design procedure described herein has been limited to the conditions outlined for the test program.

1. Selection of Fluid Film Bearing Design

Three basic bearing configurations were evaluated prior to initiation of a specific bearing design study. The three bearing designs studied were:

- Shrouded step pocket type
- Spiral groove
- Centrifugally fed hydrostatic

Each bearing configuration listed above was evaluated with regard to power

loss, lubricant flow rate, load capacity, and operating film thickness. The method applied to the analysis of these bearings is described in Reference [13] and will not be discussed here. The results of the fluid film bearing study did, however, indicate the superiority of the centrifugally-fed hydrostatic design over the other two designs considered.

Initial calculations were made for the spiral-grooved bearing with various arrangements of hydrostatic feeding and grooving and the pocketed shrouded-step bearing. The best overall design features for the spiral grooved bearing were inward pumping grooves and hydrostatic feeding at the mid-circle of the land. A comparison between the two bearing types at 10,000 rpm and 1.5×10^{-3} inch (3.81×10^{-2} mm) film thickness is summarized in Table 1.

TABLE 1

PERFORMANCE COMPARISON; POCKETED SHROUDED-STEP AND SPIRAL GROOVE BEARINGS

	Bearing Type	
Performance Parameter	Shrouded-Step Pocket	Spiral Groove
Supply Pressure, psig (Newtons/m^2)	193 (1.33×10^6)	193 (1.33×10^6)
Load, lbs. (Newtons)	2391 (1.015×10^4)	1667 (7.39×10^3)
Flow, gpm (m^3/sec)	7.88 (4.97×10^{-4})	2.06 (1.30×10^{-4})
Power Loss, hp (watts)	6.7 (4.93×10^3)	9.6 (7.06×10^3)
Temperature Rise, °F (°C)	10.3 (5.73)	56.4 (31.3)

The shrouded-step pocket bearing is superior (by a factor of 1.5) in load-carrying capacity and power loss, although it required four times the flow. The high flow rate, however, provides for less temperature rise, cooler operation, and less distortion. Although this comparison does not directly deal with temperature effects, the relative disadvantage of the spiral grooved thrust bearing would be worsened by temperature effects as a result of the lack of convective cooling indicated by its lower flow rate. Therefore, it was decided to abandon further consideration of the spiral grooved bearing and to consider the comparison between the pocketed shrouded-step and the centrifugally-fed hydrostatic bearing types.

A summary table of performance characteristics for comparison of the two designs is given in Table 2. The inlet pressures shown for the shrouded-step bearing corresponds to a nominal inlet pressure of an aircraft lube system. The inlet pressure for the centrifugally-fed hydrostatic bearing occurs downstream of the given orifice restrictors. It can be seen from Table 2 that by taking advantage of the pressure head available (centrifugal pumping) the centrifugally-fed hydrostatic bearing will carry a higher load than the pocketed-shrouded-step bearing at similar flow and power losses. In the case of the hydrostatic bearing, the outer radius was decreased slightly in order to more closely meet

TABLE 2

PERFORMANCE COMPARISON; POCKETED
SHROUDED-STEP AND CENTRIFUGALLY-FED HYDROSTATIC BEARING DESIGN

Item (Units) \ Bearing Type	Pocketed-Shrouded-Step Bearing		Centrifugally-Fed Hydrostatic Bearing	
Speed, rpm	20,000	10,000	20,000	10,000
Outer Radius, inch (mm)	3.55 (90.4)		3.50 (89.0)	
Inner Radius, inch (mm)	3.00 (76.3)		3.00 (76.3)	
Film Thickness, inch (mm)	1.5×10^{-3} (38.1×10^{-3})		1.5×10^{-3} (38.1×10^{-3})	
Inlet Temperature, °F (°C)	200 (93.5)		200 (93.5)	
Inlet Pressure, psig (Newton/m^2)	50 (3.44×10^5)		600 (4.14×10^6)	220 (1.52×10^6)
Pumping Pressure, psig (Newton/m^2)	—		1748 (1.20×10^7)	431 (2.97×10^6)
Friction Power Loss, hp (watts)	59.76 (4.5×10^4)	8.44 (6.35×10^3)	61.1 (4.61×10^3)	10.4 (7.85×10^3)
Flow Rate, gpm (m^3/sec)	9.42 (5.94×10^{-4})	4.80 (3.03×10^{-4})	9.30 (5.85×10^{-4})	4.35 (2.74×10^{-4})
Load Capacity, lbs. (Newton)	2640 (1.17×10^4)	1020 (4.54×10^3)	3360 (1.49×10^4)	1230 (5.16×10^3)
Orifice Diameter, inch (mm)	0.50 (12.7)		0.0444 (1.130)	
Number of Orifices	4		8	

the power loss requirement. Because of the appreciably higher load capacity, combined with relative design simplicity and reduced manufacturing cost, the hydrostatic bearing design was selected for test. It should be noted that the potential of obtaining higher load-carrying capacity at lower flow rates for the same bearing size is also much better with the hydrostatic than with the shrouded-step design. The hydrostatic bearing also has the advantage of being simpler to instrument.

2. Optimization of the Fluid Film Bearing

In order to optimize the centrifugally-fed hydrostatic bearing design illustrated in Figure 1, several apriori assumptions were made. Since the fluid film bearing can be optimized for only one set of operating conditions, it was first assumed that the following conditions consistent with the test program prevail:

Shaft Speed	:	20,000 rpm
Oil Viscosity	:	0.5×10^{-6} lb-sec/in^2 (1.67×10^{-7} Newton-second/m^2) MIL-L-7808E at 200°F (93.5°C)
Inner Radius of Bearing	:	2.60 inches (66.0 mm)
Maximum Available Pressure (Due to Centrifugal Pumping)	:	1100 psi (4.89×10^3 Newtons/m^2)

With the above parameters fixed, the only additional variables which remained to be varied were clearance h_f, bearing outer radius R_o, and pocket pressure P_s. The final version of the hybrid step bearing computer program was then employed to calculate bearing performance. For computation purposes, the pocket dimensions were assumed small so as to closely simulate the centrifugally fed hydrostatic design contemplated for test. The range covered by the independent variables was:

Clearance	:	0.0007 to 0.002 inches (0.0178 to 0.0508 mm)
Bearing Outer Radius	:	2.96 to 3.96 inches (75.7 to 101.3 mm)
Pocket Pressure	:	400 to 800 psi (2.76×10^6 to 5.82×10^6 Newton/m^2)

The above ranges were fixed by the physical and practical limitations imposed by the bearing system. Having established these limitations, calculations of load capacity, flow, and power loss were performed. The results of the computer runs are shown in Table 3.

The performance characteristics of a hydrostatic bearing operating within the Reynolds number range of Re = 800 to 2000 encountered in the above calculations can be shown to behave approximately according to the following expressions*:

$$\text{Load Capacity: } \frac{W}{P_s \Delta R} = \text{constant for all } h_f \qquad (1)$$

---

* These empirical relationships have been derived from the data points presented in Table 3.

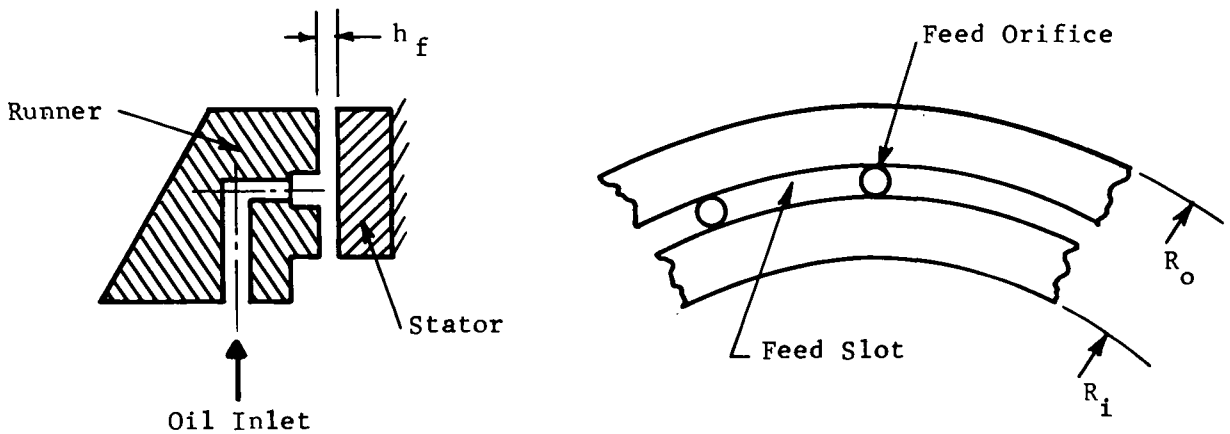

Fig. 1 Centrifugally-Fed Hydrostatic Bearing

TABLE 3

PERFORMANCE CHARACTERISTICS: CENTRIFUGALLY-FED HYDROSTATIC BEARING (COMPUTER RESULTS)

P_s		R_o		h_f		Q		Power Loss		Load		Re
lb/in^2	N/m^2	inch	mm	10^{-3} inch	10^{-3} mm	gal/min	10^{-5} m^3/sec	HP	10^4 watts	lb.	Newton	
800	5512	3.36	85.4	0.7	17.8	1.01	6.36	92.6	6.91	6259	27,840	814
				1.0	25.4	2.77	19.1	76.6	5.71			1164
				1.5	38.1	8.09	51.0	63.8	4.76			1745
				2.0	50.8	17.3	119.	57.0	4.25			2327
600	4134	3.16	80.3	0.7	17.8	1.33	9.16	60.1	4.48	4280	19,037	766
				1.0	25.4	3.67	25.3	49.6	3.70			1094
				1.5	38.1	10.8	74.4	41.2	3.07			1642
				2.0	50.8	22.9	158.	36.7	2.74			2189
		2.96	75.2	0.7	17.8	2.01	13.8	34.0	2.54	2772	12,330	718
				1.0	25.4	5.58	38.4	28.0	2.09			1025
				1.5	38.1	16.4	113.	23.1	1.72			1538
				2.0	50.8	35.0	241.	20.6	1.54			2050
		3.36	85.3	0.7	17.8	0.756	5.21	92.6	6.91	4692	20,870	814
				1.0	25.4	2.08	14.3	76.6	5.71			1164
				1.5	38.1	6.07	41.8	63.8	4.76			1745
				2.0	50.8	13.0	89.6	57.0	4.25			2327
		3.16	80.3	0.7	17.8	0.997	6.87	60.1	4.48	3200	14,234	766
				1.0	25.4	2.68	18.5	49.6	3.70			1094
				1.5	38.1	8.07	55.6	41.2	3.07			1642
				2.0	50.8	17.2	119.	36.7	2.75			2189
		2.96	75.2	0.7	17.8	1.51	10.4	34.0	2.53	2077	9,239	718
				1.0	25.4	4.19	28.9	28.0	2.09			1025
				1.5	38.1	12.3	84.7	23.1	1.72			1538
				2.0	50.8	26.2	181.	20.6	1.54			2050
400	2756	3.36	85.3	0.7	17.8	0.504	3.47	92.6	6.91	3126	13,904	814
				1.0	25.4	1.38	9.51	76.6	5.71			1164
				1.5	38.1	4.05	17.9	63.8	4.76			1745
				2.0	50.8	8.64	59.5	57.0	4.25			2327
		3.16	80.3	0.7	17.8	0.665	4.58	60.1	4.48	2140	9,519	766
				1.0	25.4	1.84	12.6	49.6	3.70			1096
				1.5	38.1	5.38	37.1	41.2	3.07			1642
				2.0	50.8	11.5	79.2	36.7	2.74			2189
		2.96	75.2	0.7	17.8	1.00	6.89	34.0	2.54	1384	6,156	718
				1.0	25.4	2.79	19.22	28.0	2.09			1025
				1.5	38.1	8.20	56.5	23.1	1.72			1538
				2.0	50.8	17.5	121.	20.6	1.54			2050

N = 20,000 rpm

μ = 0.5×10^{-6} lb-sec/in^2 (3.45 cps)

T_{in} = 200°F (93.5°C)

R_i = 2.60 in. (66.1 mm)

Flow Requirement: $$\frac{Q\Delta R}{P_s h_f^{2.6}} = \text{constant} \quad (2)$$

Power Loss $$\frac{HP\ h_f^{0.4}}{\Delta R^{1.4}} = \text{constant} \quad (3)$$

Temperature Rise: $$\frac{\Delta T\ h_f^{3} P_s}{\Delta R^{2.4}} = \text{constant} \quad (4)$$

The ΔR referred to in the above equations represents the difference between the outer and inner radii of the fluid film bearing. Because of the narrow range of outer radius variation, the assumption was also made that the mean radius remained constant.

In jet engine applications the power loss and oil flow are at a premium. These two factors must thus be carefully examined to produce the most economical trade offs.

The power loss generated by the operation of a hydrostatic bearing normally consists of two components. The loss due to shear (HP_s) and the loss due to pumping (HP_p). It can be shown that the shear losses are proportional to:

$$HP_s \sim K_1 \frac{\mu}{h_f} \quad (5)$$

Similarly, the pumping loss is proportional to

$$HP_p \sim K_2 h_f^3 P \quad (6)$$

Summing the two power losses and differentiating with respect to h, the ratio of shear to pumping power loss which would yield the lowest total combined power loss is obtained. Thus,

$$HP_t = K_1 \frac{\mu}{h_f} + K_2 h_f^3 \Delta P \quad (7)$$

$$\frac{\partial HP_t}{\partial h_f} = \frac{K_1 \mu}{h_f^2} + 3K_2 \Delta P h_f^2 = \frac{HP_s}{h_f} + \frac{3HP_p}{h_f} \quad (8)$$

Setting $\frac{\partial HP_t}{\partial h_f}$ equal to zero, the optimum ratio of shear to pumping power for purely laminar flow is approximately 3. Similarly, it can be shown that the optimum ratio of shear power loss to pumping power loss at fully developed turbulent conditions is about 6.5. The optimum power loss, however, will not necessarily occur at favorable flow conditions; hence, it is also important to establish the flow-power loss relationship.

In order to focus the optimization procedure on a specific set of operating conditions, a load capacity had to be defined; therefore, a load of 3,000 pounds (13,350 Newtons) was arbitrarily selected as a reasonable load to be carried by the fluid film bearing when the hybrid bearing is subjected to an externally-applied thrust load of 5,000 pounds (22,250 Newtons) at the maximum speed of operation. For the externally-applied load fixed at 3,000 pounds (13,350 Newtons), the data obtained in Table 3 was cross-plotted and reproduced for constant loading conditions as shown in Table 4.

The pumping power required to provide oil flow was calculated for each condition and added on to the shear losses. The data was calculated for a limited range of practically reasonable clearances, outer radii, supply pressures and a constant oil temperature of 200°F. No iterations to correct the viscosity to a mean film temperature were made. Note that the pumping power is based upon the maximum supply pressure of 1100 psi (7.58×10^6 Newtons/m^2) corresponding to 20,000 rpm operation. A graph representing the relative effects of flow as a "trade off" for power loss is shown in Figure 2. Examining the trends it is of importance to note that at least within the lower bearing size range, the flow can apparently be subjected to wide variation without an appreciable effect on power loss.

A low flow limit beyond which the power loss begins to increase significantly appears to be occurring at about Q = 5 gpm (3.15×10^{-4} m^3/sec). Combining this low flow limit with the lowest power dissipation desired, it is apparent that the optimum bearing geometry is represented by the R_o = 3.02 (76.6 mm) bearing operating at an 0.001 inch (0.0254 mm) clearance. Although the temperature rise of 89°F (49.5°C) at these conditions appears somewhat high considering the 200°F (93.5°C) oil inlet temperature, this rise can still be tolerated.

3. Test Bearing Geometry Selection

The geometry presented previously, although being representative of a reasonable optimized geometry, was not chosen for the final fluid film bearing geometry to be tested. The significant reasons for the selection of a geometry other than the one previously discussed was to provide the following:

1. The added safety of testing at larger film thickness.
2. Larger nominal operational film thicknesses to allow a greater margin for manufacturing tolerances.
3. Higher load capacity at low test speeds.
4. The increased power requirement for a bearing with an increased radius is not critical for testing purposes.

Based on the reasoning outlined above, a bearing having an outer radius of 3.16 inches (80.5 mm) operating at a clearance of 0.0015 inches (0.0381 mm) was selected for the test configuration. Its performance characteristics at 20,000 rpm are given in Table 4.

A comparison between the bearing with an outer radius of 3.02 inches (76.6 mm) and the bearing with a 3.16 inch (80.5 mm) radius, both operating at 10,000 rpm, is shown in Table 5.

TABLE 4

PERFORMANCE CHARACTERISTICS: CENTRIFUGALLY-FED
HYDROSTATIC BEARING – INTERPOLATED RESULTS*

P_s		R_o		h_f		Q		Pumping Power		Friction Loss		Total Power		Temp. Rise	
lb/in^2	N/m^2	Inch	mm	10^{-3} inch	10^{-3} mm	gpm	10^{-4} m^3/sec	hp	10^2 watts	hp	10^2 watts	hp	10^2 watts	^oF	^oC
800	5512	3.02	76.7	0.8	20.3	3	18.9	1.91	14.3	39.0	291	41	306	165	91.7
				0.9	22.9	4	25.2	2.54	18.9	37.0	276	39.5	295	119	66.1
				1.0	25.4	5	31.5	3.20	23.9	34.0	254	37.2	277	89	49.4
				1.1	27.9	6.5	40.9	4.15	30.9	32.5	242	36.6	273	67.5	37.5
				1.2	30.5	8.0	50.4	5.10	38.0	31.5	235	36.6	273	55.0	30.5
				1.3	33.0	10	63.0	6.4	47.7	30.0	224	36.4	271	43.5	24.2
700	4823	3.08	78.2	1.0	25.4	3.9	24.6	2.5	18.7	40.0	298	42.5	317	130	72.2
				1.2	30.5	6.3	39.7	4.0	39.8	38.0	283	42.0	313	79.5	44.2
				1.4	35.6	9.3	58.6	5.9	44.0	35.0	261	40.9	305	52.3	29.0
				1.6	40.6	13.5	85.1	8.7	64.9	31.5	235	40.2	250	36	20.
				1.8	45.7	18.4	115.9	11.7	87.3	30.0	224	41.7	311	27	15.
				2.0	50.8	23.8	137.3	15.2	113.	29.5	220	44.7	333	22.5	12.5
600	4134	3.16	80.3	1.0	25.4	2.7	17.0	1.7	12.7	50.0	373	51.7	386	228	127
				1.2	30.5	5.0	31.5	3.2	23.9	46.5	347	48.7	363	118	65.
				1.4	35.6	7.0	44.1	4.5	33.6	43.5	325	48.	358	124	68.9
				1.5	38.1	8.1	51.0	5.1	38.0	41.2	307	46.3	345	68	37.8
				1.7	43.2	12.0	75.6	7.7	57.4	40.0	298	47.7	356	48	26.7
500	3445	3.25	82.6	1.6	40.7	7.5	47.3	4.8	35.8	50.0	373	54.8	409	87	48.3
				1.7	43.2	8.6	54.2	5.5	41.0	49.5	369	55.0	410	77	42.8
				1.8	45.2	9.3	58.6	5.9	44.0	48.5	362	54.4	406	70	38.9
				1.9	48.3	11.2	70.6	7.2	53.7	47.0	350	54.2	404	58	32.2
				2.0	50.8	12.2	76.9	7.8	58.2	46.0	343	53.8	401	53	29.4
400	2756	3.42	86.9	2.0	50.8	9.0	56.7	5.75	42.9	62.0	463	67.7	505	90	50
				2.1	53.3	9.5	59.9	6.1	45.5	60.0	448	66.1	493	83	46.1
				2.2	55.9	10.5	66.2	6.7	49.9	58.0	433	64.7	483	73	40.6

*N = 20,000 rpm

W = 3,000 lbs. (13,344 Newtons)

μ = 0.50×10^{-6} lb-sec/m^2 (1.67×10^{-7} Newton-second/m^2)

T_{in} = 200^oF (93.5^oC)

R_i = 2.60 in (66.1 mm)

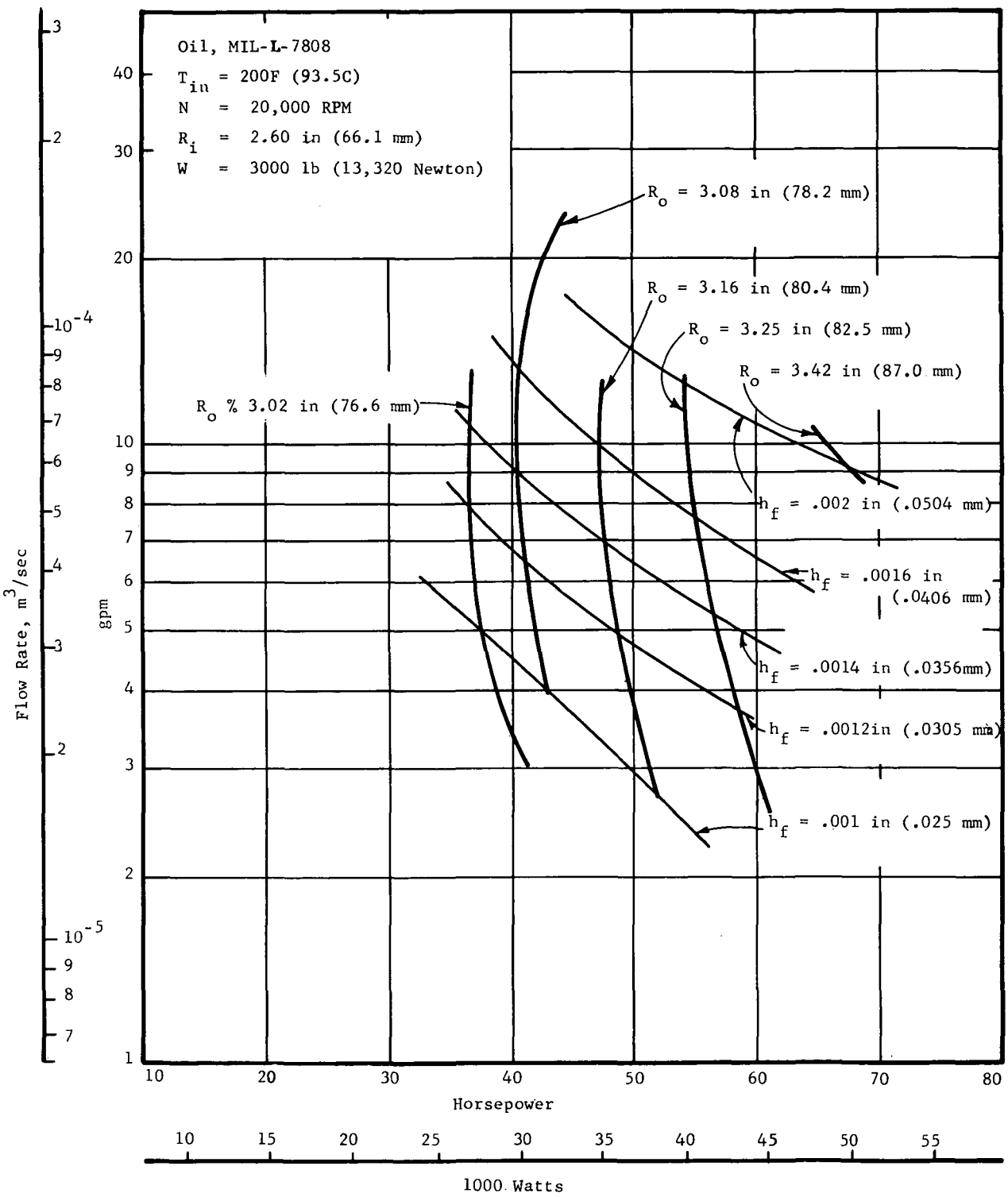

Fig. 2 Power Loss; Centrifugally-Fed Hydrostatic Bearing

TABLE 5

COMPARISON OF CENTRIFUGALLY-FED HYDROSTATIC BEARING FOR VARYING OUTER RADIUS

N = 10,000 rpm

R_o in (mm)	R_i in (mm)	h_f 10^{-3} in (mm)	P_s lb/in^2 (10^3 K/m^2)	W lb (N)	Power Loss HP (watts)	Flow gpm 10^{-3} m^3/sec	ΔT °F (°C)	d_o in (mm)
3.02 (76.6)	2.60 (66)	1.0 (.0254)	235 (1619.)	870 (3870.)	6.8 (5080)	1.53 (9.64)	45.2 (25.1)	0.052 (1.32)
3.16 (80.5)	2.60 (66)	1.5 (.0371)	200 (1378.)	1012 (4501.)	7.22 (5390)	3.24 (20.4)	26.7 (14.8)	0.0460 (1.17)

It should be noted that the flow through the restrictors is calculated on a separate basis. Once the orifice restriction has been determined based upon the 20,000 rpm point, the same orifice restriction d_o is utilized in the 10,000 rpm comparison, so as to reflect the fixed bearing geometry. As can be seen, at 10,000 rpm the load-carrying-capacity of the 3.16 inch (80.5 mm) bearing is about 25 percent higher than that of the 3.02 inch (76.6 mm) bearing with a clearance of approximately 1.5×10^{-3} inch (0.0371 mm) for the larger radius bearing versus 1.0×10^{-3} (0.0254 mm) for the smaller radius bearing. The power losses due to shear are comparable. The flow for the smaller size bearing is low because of the low clearance. This, in turn, results in a temperature rise of approximately two to one for the smaller bearing over that of the larger one.

The 3.16 inch (80.5 mm) bearing selected does offer the enlarged operating clearances and higher load capacity at lower speeds which make it preferable for test purposes over the more optimum geometry reflected by the smaller size bearing. An overall performance map for the fluid film bearing is shown in Figure 3. The anticipated performance for the fluid film bearing in terms of load capacity and flow rate is obtained from the data at the intersection of any film thickness curve and speed curve.

In general, the load-carrying capacity of the fluid film bearing is extremely low at film thicknesses in excess of 3.0×10^{-3} inch (0.0763 mm). The capacity is also negligibly low at speeds below 5,000 rpm over the full film thickness range. From the standpoint of jet engine operation this is not a detriment. Fluid film thickness in excess of 3.0×10^{-3} inch (0.0763 mm) are impractical since in addition to low load-carrying capacity the flow requirements are prohibitively large. Furthermore, a speed of 5,000 rpm is too low to enter into consideration in high-speed engine design.

Because substantial temperature rises are anticipated at high speed operation, the analytical data was generated for oil temperatures of 200°F (93.5 °C) and 300°F (147°C).

Test Ball Bearing Analyses

The ball bearing component of the hybrid boost bearing system, as supplied by NASA, had previously been utilized by another NASA contractor for evaluation testing. This bearing is a 125 mm bore, angular contact, split inner race bearing manufactured to the dimensions listed in Table 6.

The ball bearing was analyzed with the aid of a computer program developed by Mr. A. B. Jones, based on the model shown in Figure 4. For calculation purposes, the outer bearing ring is assumed fixed in space and all inner race deflections are calculated relative to the outer race and referred to the orthogonal x-y-z coordinate system as indicated.

A series of ball bearing performance calculations, based on the data listed in Table 6, were made for speeds of 0, 10,000, 15,000, and 20,000 rpm at axial loads of 500, 1,000, 3,000, and 5,000 pounds. A radial load of 80

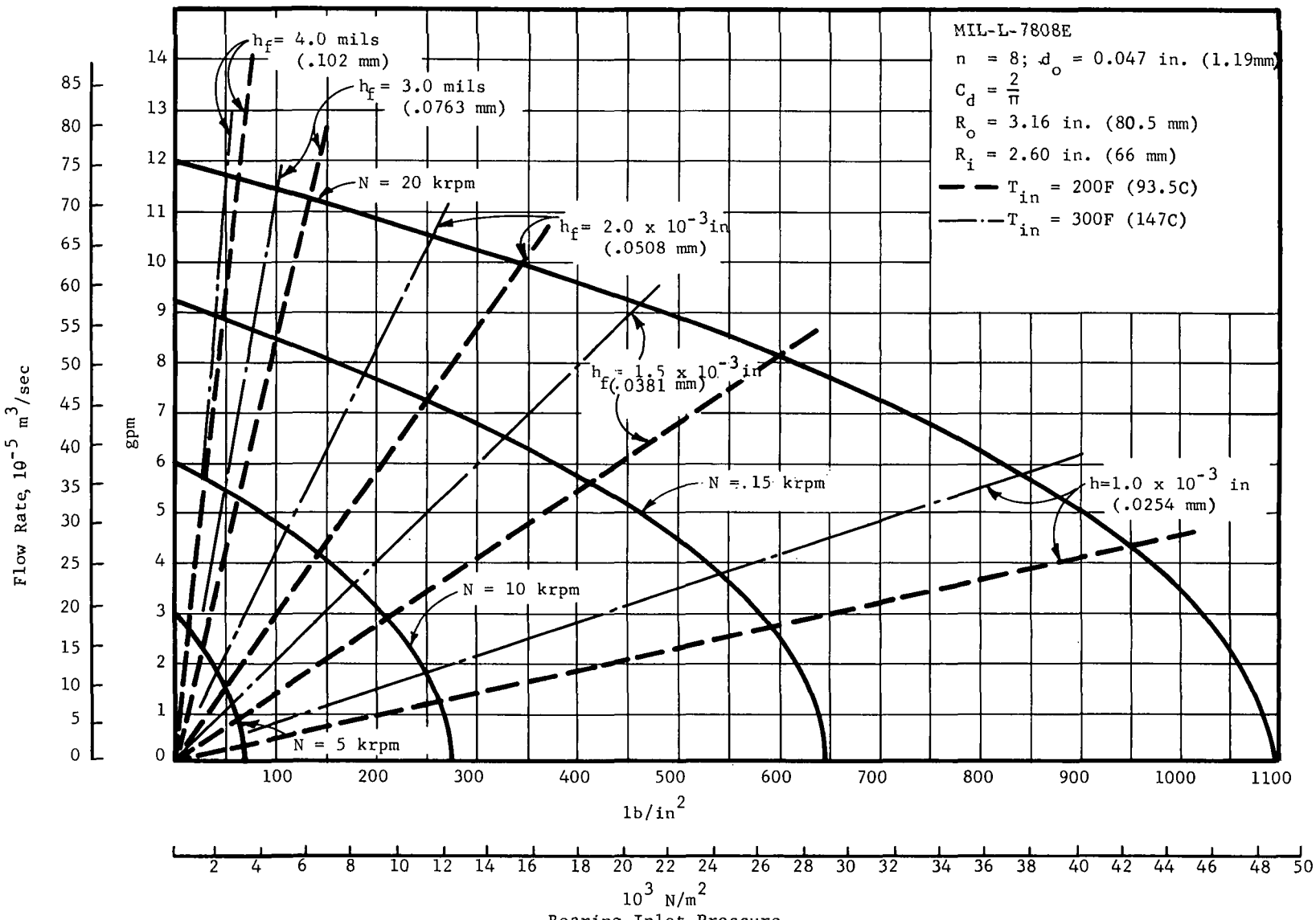

Fig. 3 Fluid Film Bearing - Analytical Performance Map

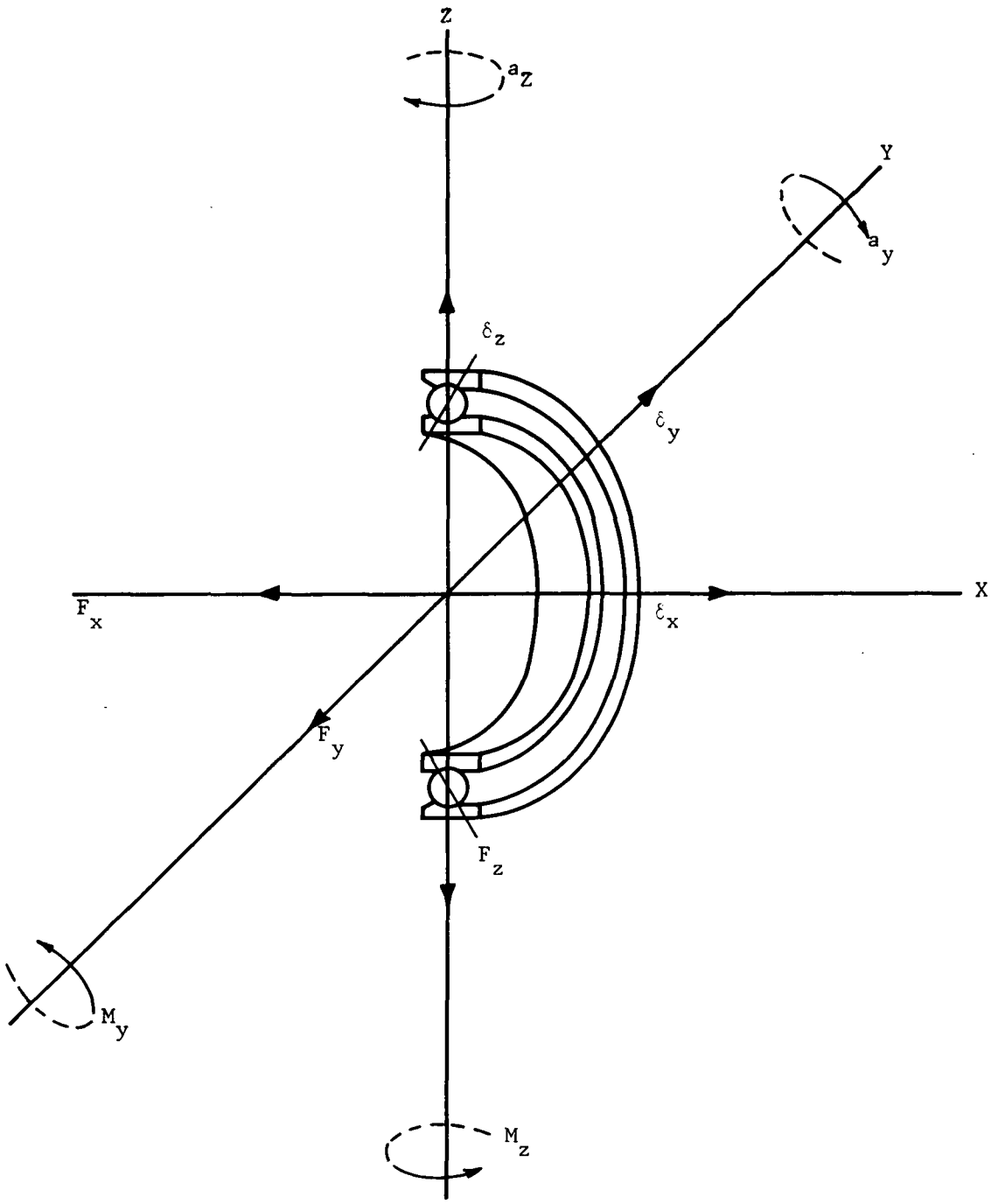

Fig. 4 Ball Bearing Analytical Model (Indicated Directions are Positive)

pounds was assumed constant for all conditions. This assumed weight compares favorably with the measured radial bearing load of 82 pounds. The effect of centrifugal growth of the inner race, and initial interference fit, were not included in this first trial at calculating the ball bearing performance. As will be shown later, the displacement between bearing races under a given thrust load is affected to a significant extent by the changes in the internal bearing clearance resulting from high interference fits, centrifugal growth and thermal gradients.

TABLE 6

TEST BALL BEARING PROPERTIES

Diameter, Outer	:	7.8000 inches (196 mm)
Diameter, Inner	:	4.9210 inches (125 mm)
Diameter, Pitch	:	6.2008 inches (157.5 mm)
Width	:	1.280 inches (32.55 mm)
Race Curvature, Outer	:	0.52
Race Curvature, Inner	:	0.52
Number of Balls	:	21
Ball Diameter	:	0.8125 inch (20.65 mm)
Material - Balls & Races	:	M-50 at Rc 60
Material - Cage	:	AMS 6415 at Rc 28/32
Cage Treatment	:	AMS 2412 Silver Plate
Initial Contact Angle	:	24 degrees

Performance data output from the ball bearing computer program is extremely detailed and quite lengthy, therefore, only pertinent design information listed in Table 7 was selected for presentation in this report.

The performance factor pertinent to the design of the hybrid boost bearing is the load-speed-deflection characteristic of the ball bearing. This characteristic, plotted on Figure 5, is typical for high-speed bearings. All bearing displacements are shown relative to the initial contact angle displacement position, hence, the displacement at zero speed and zero load serves as the zero reference.

As bearing speed increases, relative ring displacement is in a direction opposite to the displacement due to a load increase. These negative displacements occur as a result of the increase in radial inertia forces of the bearing balls. The increased inertia forces load the balls against the outer race and subsequently change the outer race contact angle. This behavior must be taken into consideration in the design of the hybrid boost bearing.

As the design progressed, it became apparent that changes in internal bearing clearance due to both the interference fit of the inner race and to inner race centrifugal growth are significantly large and must be accounted for in the calculations. The extent of thermal gradient effects on the bearing internal clearance could not be readily determined and was thus not taken into consideration in the calculations.

Measurements of the contact angle of the bearing to be employed in the testing disclosed a significant difference between the nominal, design point contact angle and the measured one. As was indicated above, the nominal contact angle was given at 24 degrees; the measured angle turned out to be 27.7 degrees. Because of this, the bearing performance was recalculated. At this

TABLE 7

CALCULATED BALL BEARING DEFLECTION DATA

Speed rpm	Load lb (Newtons)	β_i	β_m	P_d 10^{-3} in (mm)	$P_E/2$ 10^{-3} in (mm)	δ_x * 10^{-3}in (10^{-3}mm)	δ_B ** 10^{-3}in (10^{-3}mm)	δ_f *** 10^{-3}in (10^{-3}mm)
20 K	5 K (22240.)	27.7°	20.58°	4.15 (.0105)	11.425 (.0291)	1.80 (43.2)	0.34 (8.64)	-2.39 (-60.7)
	3 K (13344.)					.47 (11.9)	-1.00 (-25.4)	-3.73 (-94.7)
	1 K (4448)					-1.20 (-30.5)	-2.66 (-67.6)	-5.39 (-137)
15 K	5 K (22240)		21.8°	4.65 (.0155)	12.07 (.0317)	2.08 (52.8)	1.26 (32.0)	-1.47 (-37.3)
	3 K (13344)					0.91 (23.1)	0.09 (2.29)	-2.64 (-67.1)
	1 K (4448)					-1.13 (-28.7)	-1.95 (-49.5)	-4.68 (-119)
10 K	5 K (22240)		22.7°	5.03 (.0128)	12.535 (.0319)	2.56 (65.0)	2.21 (56.1)	-0.52 (-13.2)
	3 K (13344)					1.58 (40.1)	1.23 (31.2)	-1.50 (-38.1)
	1 K (4448)					-0.62 (-15.7)	-0.97 (-24.7)	-3.70 (-94)
0 K	5 K (22240)		23.4°	5.33 (.0135)	12.888 (.0327)	2.73 (69.3)	2.73 (69.3)	0 (0)
	3 K (13344)					2.02 (51.3)	2.02 (51.3)	-0.71 (-18.0)
	1 K (4448)					1.04 (26.4)	1.04 (26.4)	-1.69 (-42.9)

* δ_x Measured from mounted contact angle at speed.

** δ_B Referenced back to mounted contact angle at zero speed = $(P_{Ex} - P_{E23.4})/2 + \delta_x$

*** δ_f Deflection from mounted reference = δ_B - (2.73), reference at zero speed and 5000 lb. (22240 Newton) axial load setting.

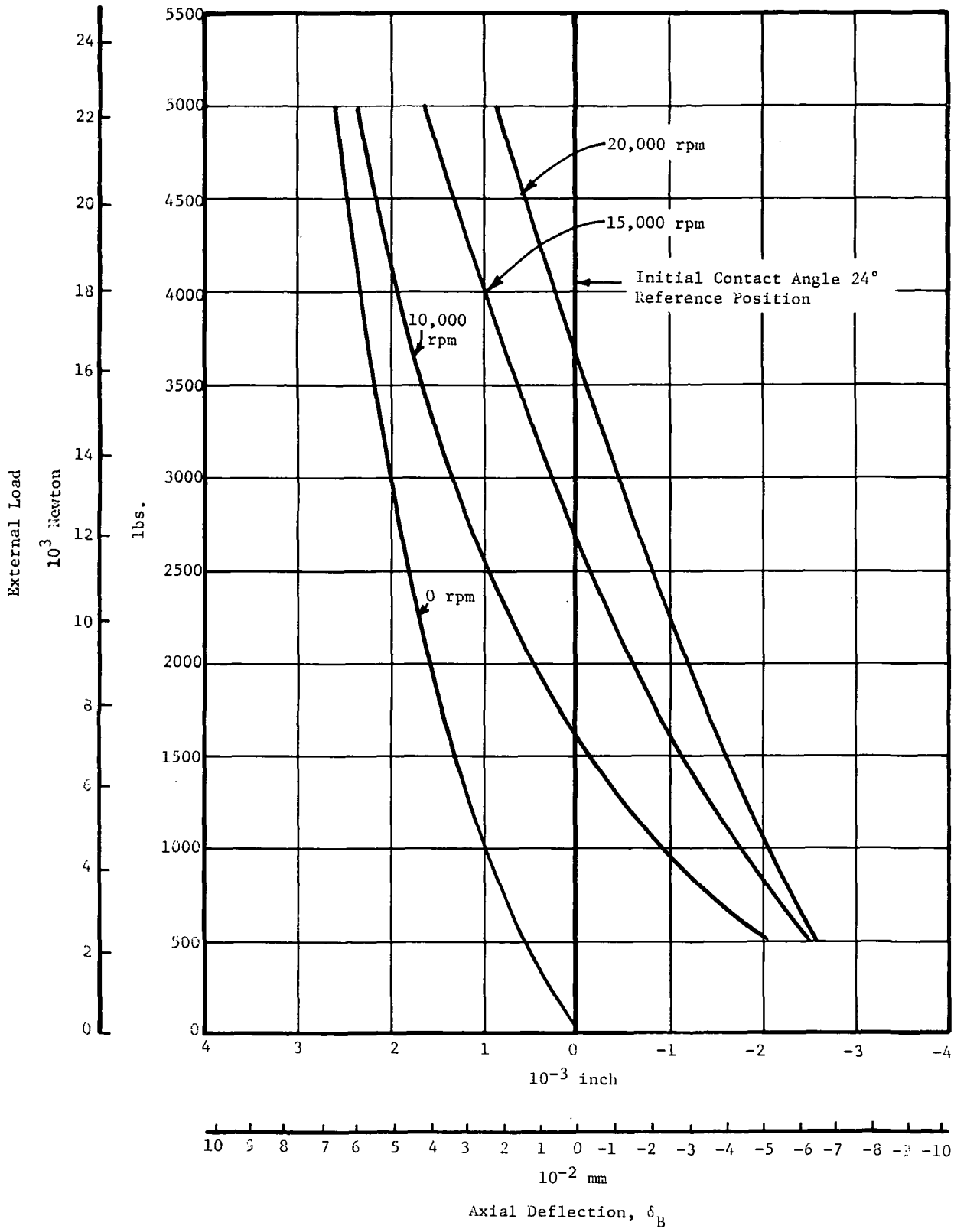

Fig. 5 Ball Bearing-Load vs. Deflection Curves for Constant $\beta_i = 24^o$

stage initial inner race interference and centrifugal growth effects were also accounted for. The procedure here employed was to calculate the change in the ball bearing radial play as a function of speed and the initial interference fit using in-house computer programs. The calculated change in clearance was then used as an additional input to the RECAP program. With the incremental change in internal clearance as an input, the program calculates the true contact angle and produces output data that is representative of the steady-state ball bearing performance at any given speed and load.

The deflection characteristics of the test ball bearing are plotted in Figure 6 using the initial contact angle position of the "as installed on the rotor" bearing at zero speed as reference. Differences among the "as installed" contact angles at different speeds are due principally to centrifugal growth of the inner race.

All the deflection data for this bearing are given in Table 7. An additional factor, δ_f is here introduced to facilitate the establishment of the thickness of the shim required for hybrid operation. The symbol δ_f denotes the distance between the inner and outer race (i.e., gap between the rotating and stationary fluid film bearing components) taken with reference to the zero speed and 5,000 pound (22,240 Newtons) load condition.

Combined Fluid Film Ball Bearing Performance

The basic hybrid boost bearing concept has been discussed in Reference [8]. Figure 7 shows a schematic diagram of this concept taken from the given reference. Neglecting the radial stiffness of the ball bearing, the system is described as consisting of three springs arranged in a series - parallel pattern. The three springs identified are those of the preload spring, ball bearing, and fluid film bearing, respectively. The preload spring stiffness K_S is in series with the ball bearing stiffness K_B, thus, the equivalent stiffness K_e of the rolling element bearing is given by the expression:

$$\frac{1}{K_e} = \frac{1}{K_S} + \frac{1}{K_B} = \frac{K_B + K_S}{K_S K_B} \tag{9}$$

This expression holds for the conditions where $\delta_s < \delta_{s\ max}$ (Figure 7); that is, while the preload spring is not fully deflected. Once the preload spring is bottomed, the equivalent stiffness becomes

$$K_e \approx K_B \tag{10}$$

Since the fluid film bearing stiffness K_F is in parallel with the equivalent ball bearing stiffness, the overall effective hybrid bearing stiffness K'_e is given by the expression:

$$K'_e = K_e + K_F = \frac{K_S K_B}{K_S + K_B} + K_F \tag{11}$$

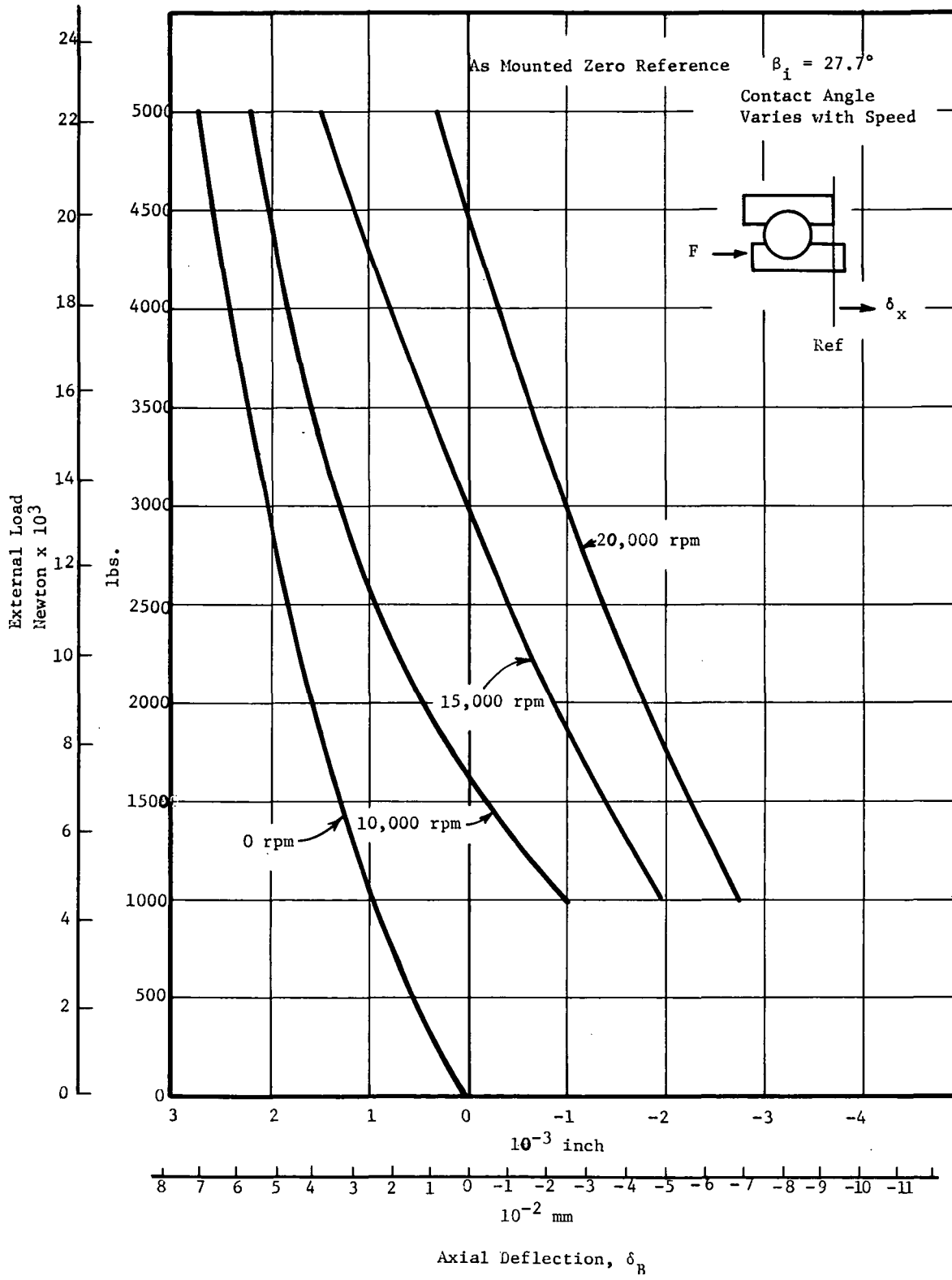

Fig. 6 Ball Bearing Load vs. Deflection Curves

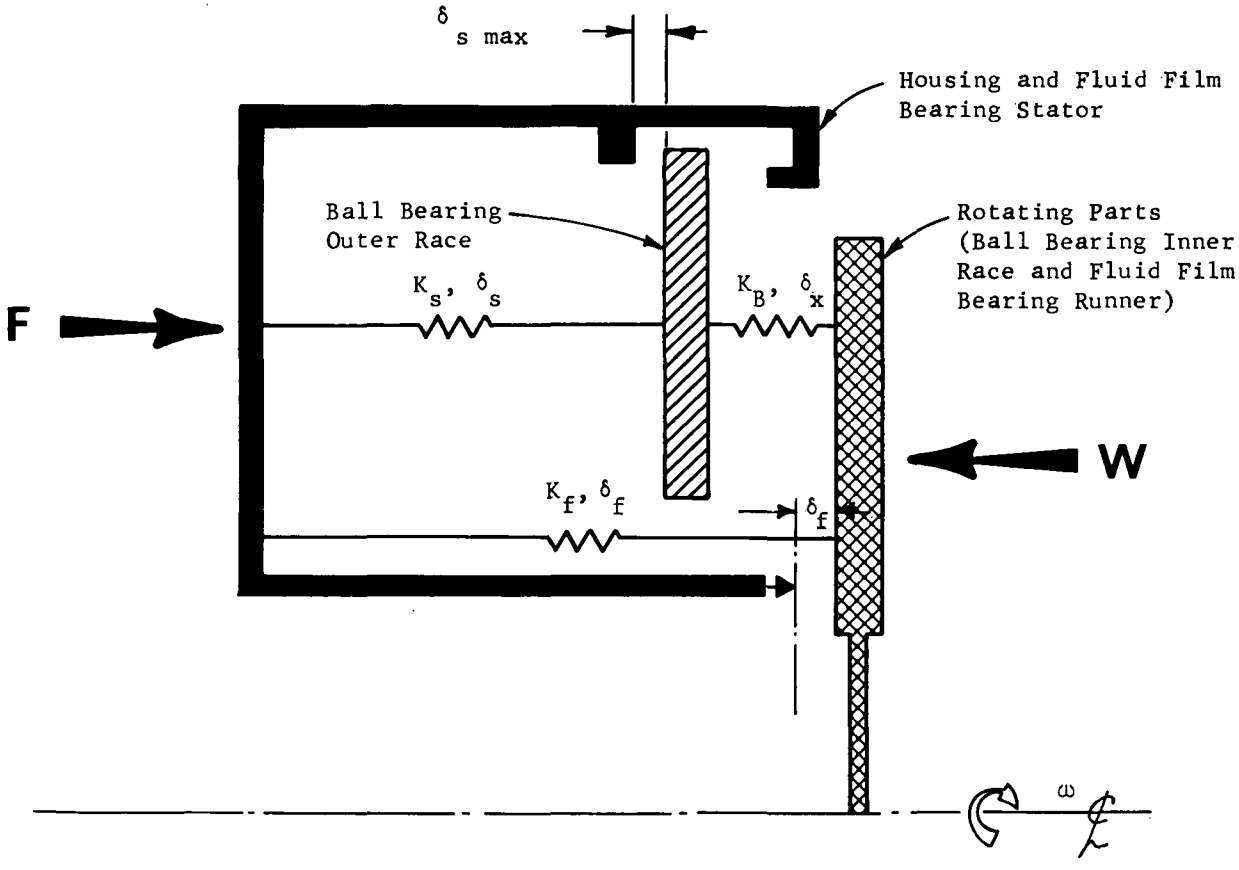

K_s, δ_s = Preload Spring Stiffness and Deflection

K_B, δ_x = Ball Bearing Axial Stiffness and Deflection

K_f, δ_f = Fluid Film Bearing Stiffness and Deflection

Fig. 7 Hybrid Boost Bearing Schematic

Again, this expression is valid only where $\delta_s < \delta_{s\ max}$. For the case where the preload spring is bottomed ($\delta_s = \delta_{s\ max}$):

$$K'_e = K_f + K_B \tag{12}$$

Because of the nonlinear characteristics of both the fluid film bearing and the ball bearing stiffnesses, the performance characteristics of the combined hybrid boost bearing are best presented in graphical form. The graphical representation of the hybrid boost bearing load-film thickness relationship is shown in Figures 8 through 10.

The relative positions of the fluid film and ball bearing are established by locating the two components so that the clearance of the fluid film bearing is at a prescribed value at static conditions. The static conditions are selected as a reference because the clearance tends to be at its lowest levels when the unit is either nonrotating or rotating at low speeds. Since the fail safe aspects of the hybrid bearing must be taken into consideration, a reasonable clearance between the stationary and rotating parts of the fluid film bearing is provided to avoid seizure when testing for oil loss.

In order to demonstrate the effect of "fail safe" considerations on hybrid bearing performance, the hybrid bearing performance characteristics were determined for two different sets of conditions, each one denoting a different "fail safe" setup clearance condition.

To bring about a favorable load distribution, low setup clearances are required. The first hybrid bearing setup was thus assumed to contain a static clearance of 0 mils at the reference point of 5,000 pounds and zero speed.

Having established the reference point for the fluid film ball bearing components, the load versus deflection characteristics for each bearing are combined and numerically added to yield the equivalent load-versus-deflection curve for the hybrid boost bearing at each of the given sets of conditions. These curves are shown in Figures 8 through 10 for speeds of 10,000, 15,000, and 20,000 rpm respectively.

In Figure 8 at an externally-applied load of 5,000 pounds (22,240 Newtons) (Point A), the load carried by the ball bearing is 3,600 pounds (Point B) and that carried by the fluid film bearing 1,400 pounds (Point C). Should the fluid film bearing fail because of loss of oil, the full load is still safely carried under ideal conditions by the ball bearing at a clearance between the fluid film bearing rotating and stationary parts of 0.52×10^{-3} inch (0.012 mm) while the speed remains at 10,000 rpm. Should, however, the speed drop to zero while the full load of 5,000 pounds remains applied to the bearing, seizure may occur.

The second set of curves presented in Figures 8 through 10 assumes a static clearance of 1.48×10^{-3} inches (0.039 mm) at zero speed and 5,000 pounds (22,100 Newtons) to provide sufficient fail safe clearance at this condition. The net effect of this increased fail safe spacing is to drastically diminish the share of load carried by the fluid film bearing.

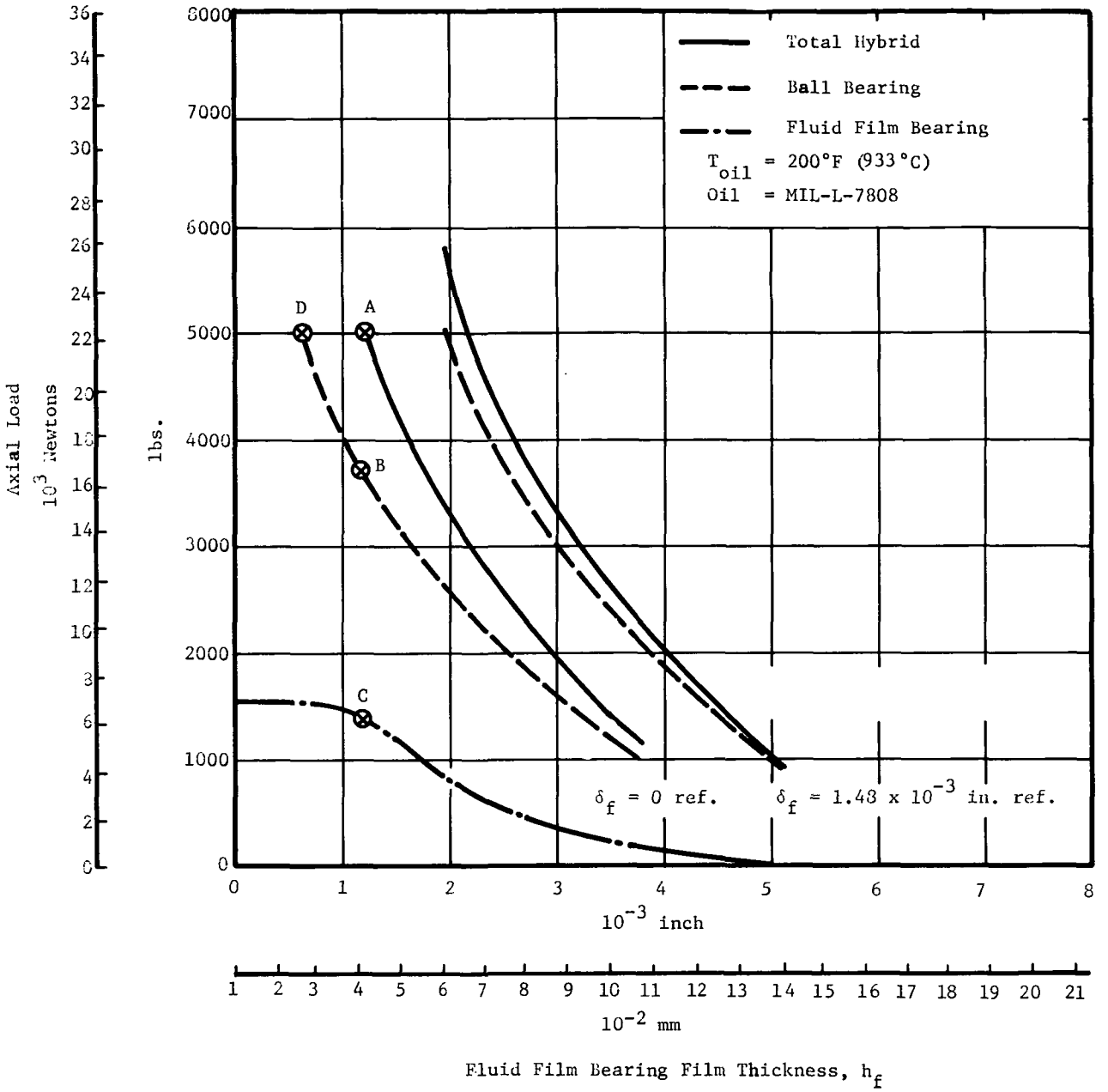

Fig. 8 Performance Characteristics of Hybrid Boost Bearing at 10,000 rpm

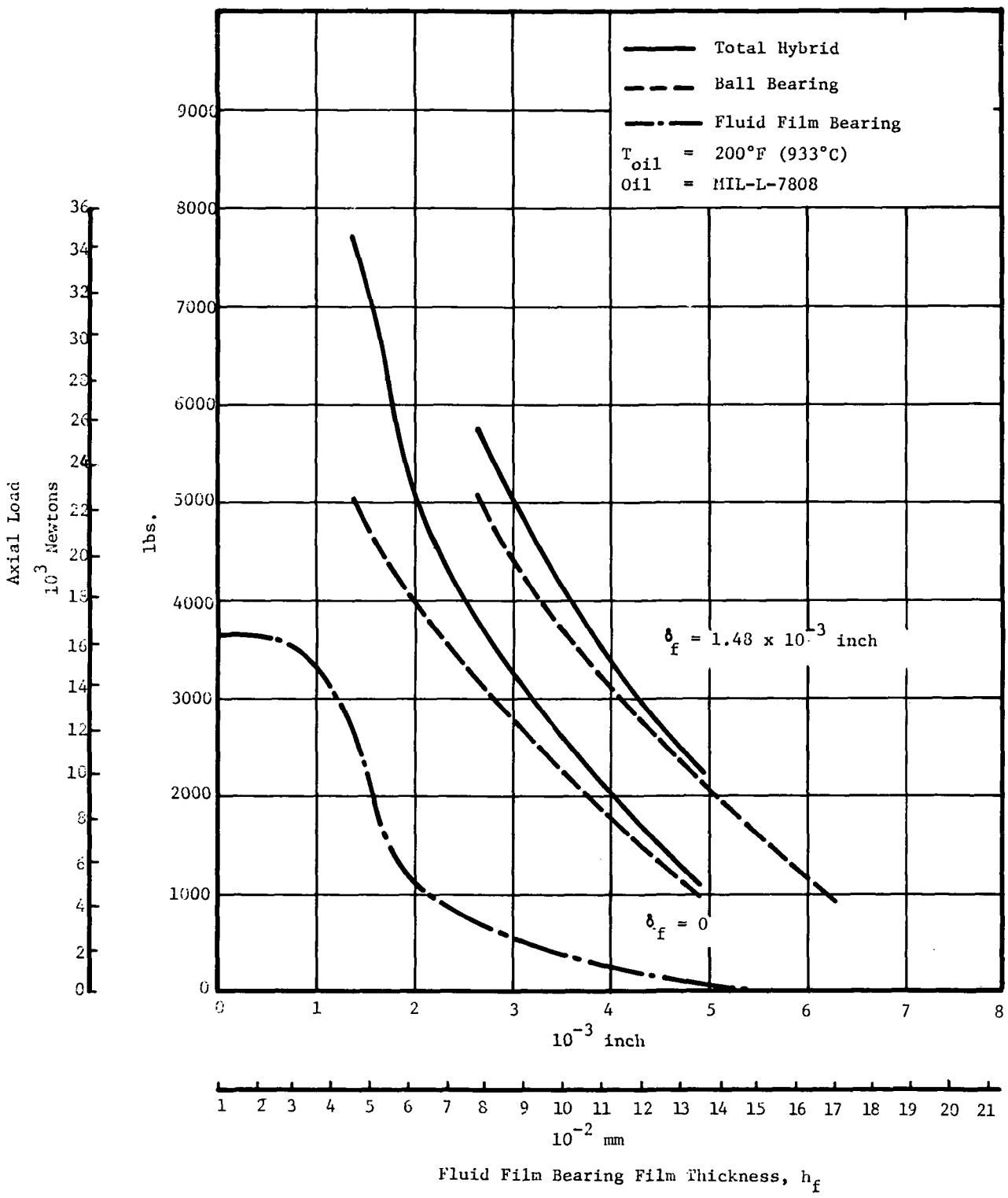

Fig. 9 Performance Characteristics of Hybrid Boost Bearing at 15,000 rpm

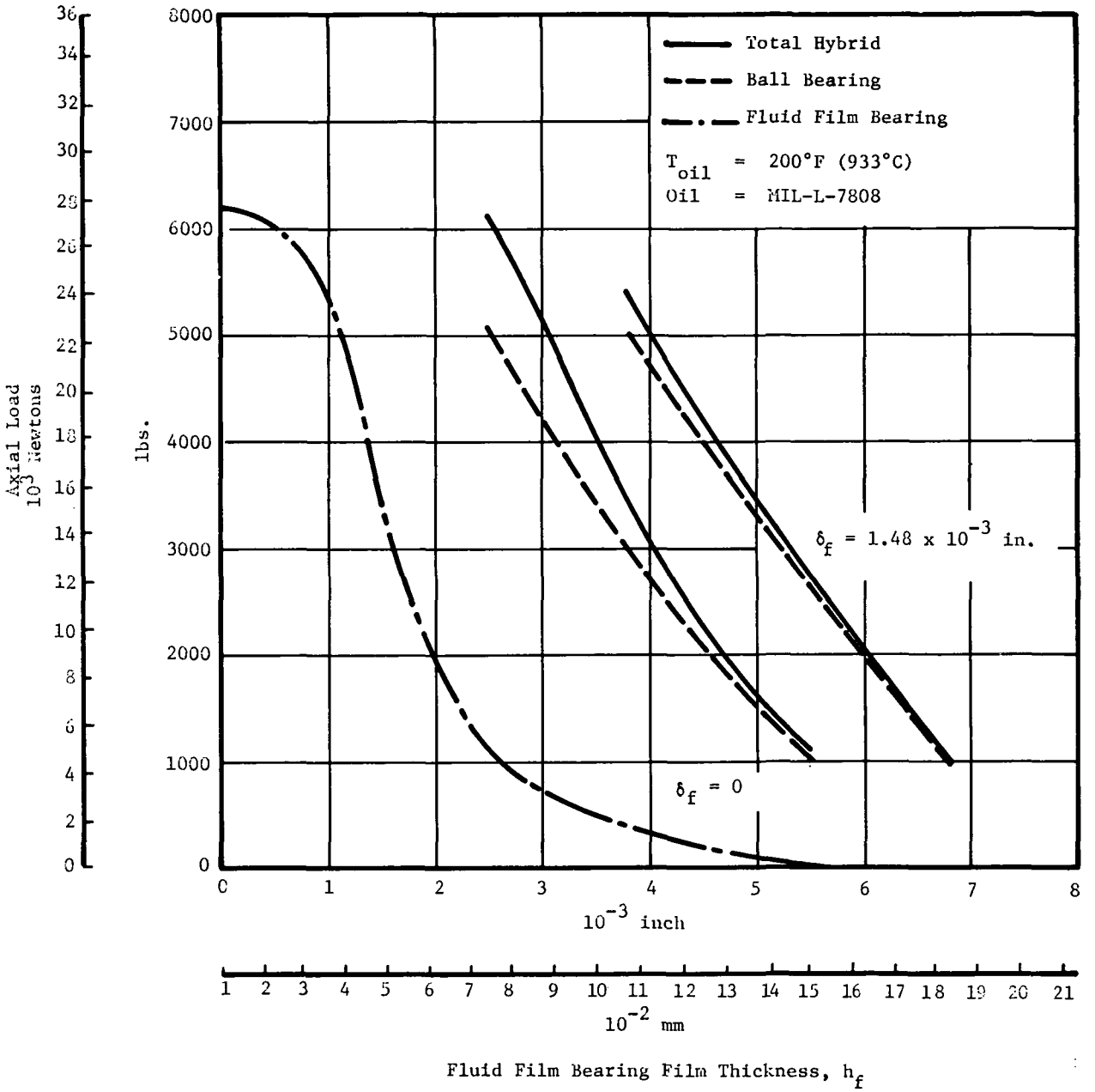

Fig. 10 Performance Characteristics of Hybrid Boost Bearing at 20,000 rpm

The performance characteristics shown in Figures 8 through 10 also indicate that as the speed goes up, the load sharing becomes adversely affected; hence, in order to obtain the highest possible load on the fluid film bearing the fail safe aspects must either be limited to the operational speed or special provisions made to avoid seizure [9]. Reduction in the ball bearing stiffness and increase in fluid film bearing stiffness could help to further equalize the load-sharing aspects of the hybrid boost bearing configuration discussed in this section. Considering the fact that a given ball bearing was supplied, stiffness reduction was not feasible within the scope of this program. The fluid film bearing was optimized at a given load with respect to power loss and flow. No attempt was made to further optimize the stiffness.

TEST FACILITY

The test facility in which the hybrid boost bearing performance was evaluated consisted of a test rig, auxiliary systems such as the drive, loading, and lubrication, and both test and facility monitoring instrumentation.

Detailed descriptions of each major facility component is provided in Reference [10]. Within the scope of this program some modifications had to be made to provide oil flow into the shaft center for bearing lubrication. The facility was furthermore altered for remote control operation and the test head designed to fit the given requirements.

Test Rig Design

The hybrid boost test rig design which formed the basis for a preliminary design analysis is illustrated in Figure 11. This design, although providing sufficient structural rigidity for sustaining a 5,000 pound (22,240 Newton) axial load, indicated a potentially broad region of critical speeds within the speed range to be used during test procedures. The problem associated with test rig operation within the region of critical speeds specified for the rig design illustrated in Figure 11 was substantially reduced with the introduction of a flexible bearing mount in conjunction with an oil-lubricated hydrostatic bearing located between the test ball bearing cartridge and the outer housing.

The objective in using the flexibly-mounted hybrid boost bearing was to favorably alter the system resonances and lessen the effects of vibration amplitudes at or near any system critical.

Figure 12 shows how the hydrostatic bearing and its radial flexure support isolates the ball bearing retainer from the test rig housing and introduces lowered stiffness and increased damping to the system. The radial flexure support arrangement combines high axial stiffness and low stress levels for accepting loads up to 5,000 pounds (22,240 Newtons) with a relatively soft radial stiffness to allow stable operation of the overhung bearing system.

The combination of the flexure-supported hydrostatic damper bearing and the

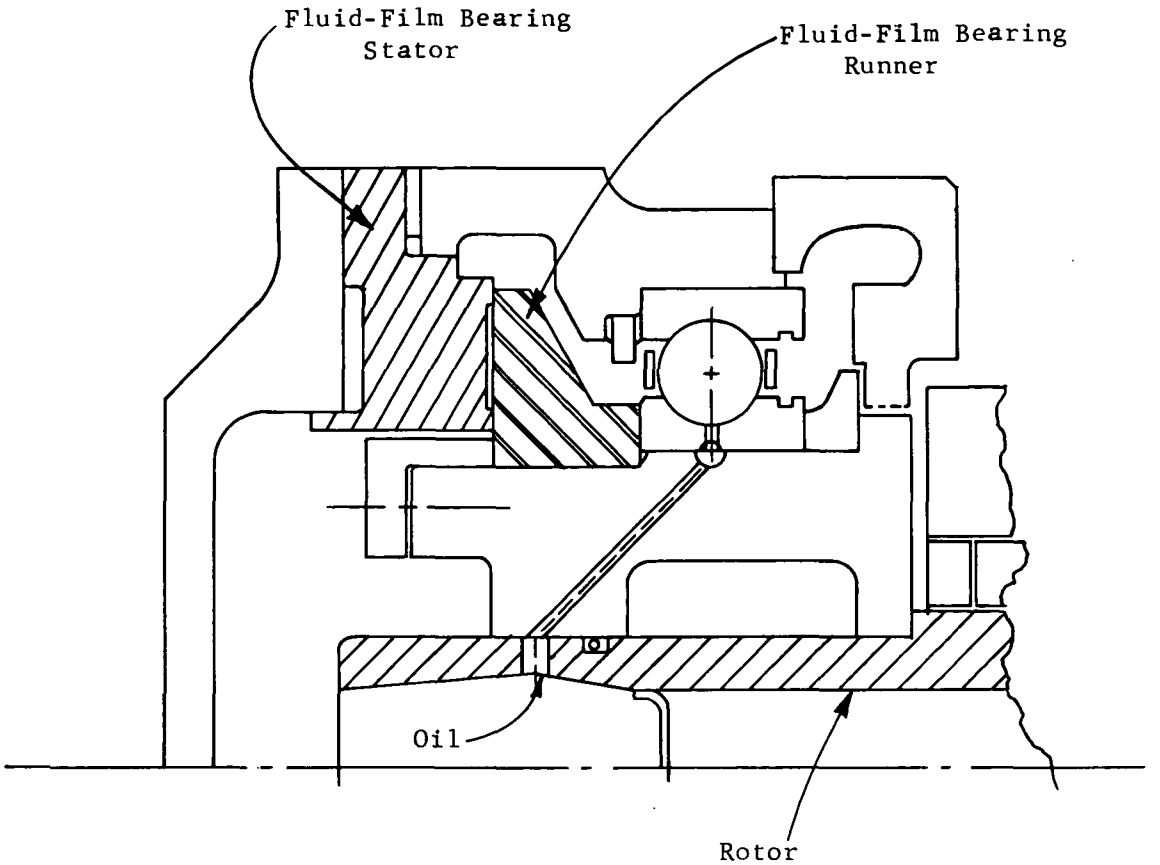

Fig. 11 Hybrid Bearing-Preliminary Design

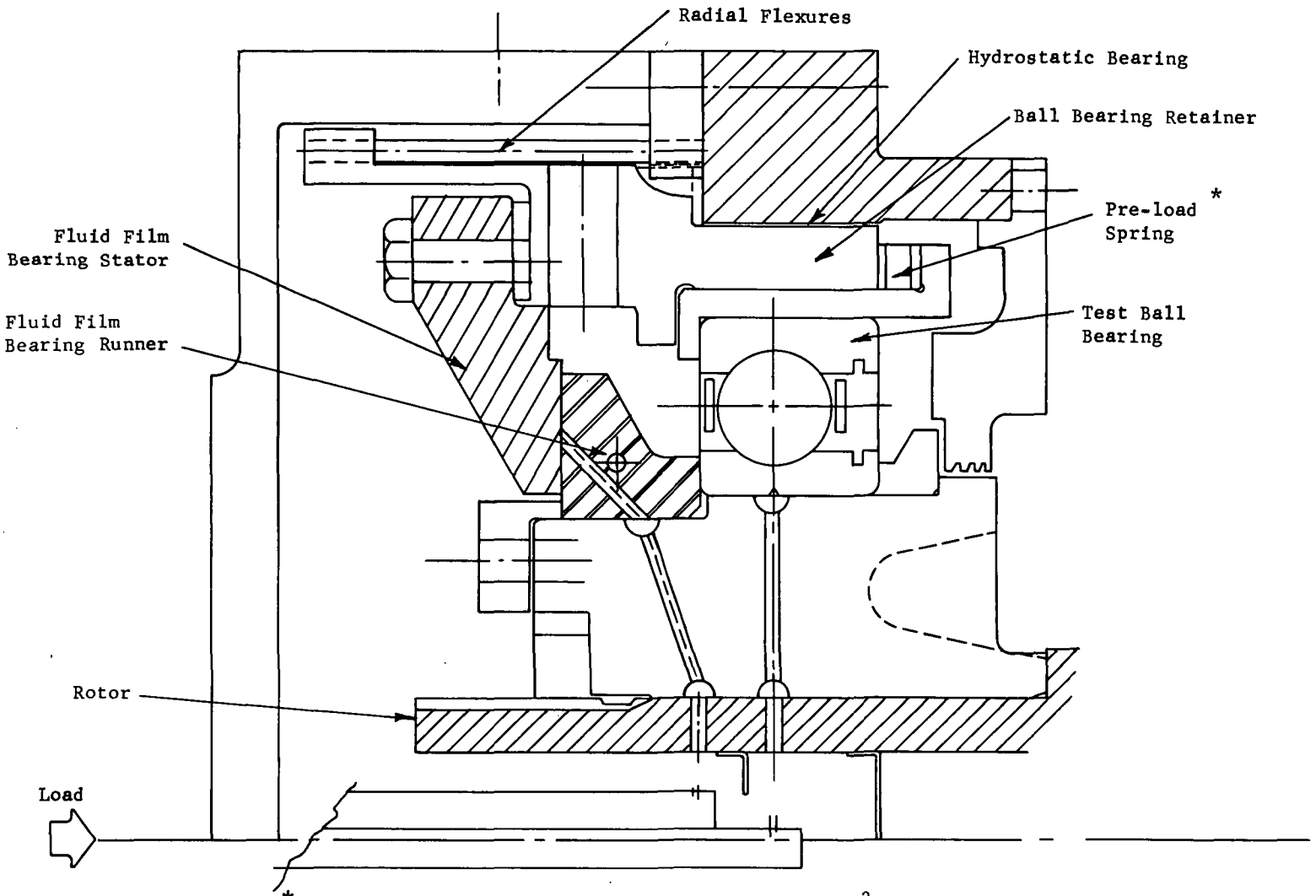

Fig. 12 Flexure Supported Hybrid Bearing Including Damper Bearing

hybrid boost bearing was subjected to a final evaluation to determine possible difficulties with component stress, critical speed, or rotor response. The final configuration which was subjected to analysis is illustrated in Figure 13 which shows the entire test rig including the support spindle. For reference, a picture of the radial flexure mount is shown in Figure 14.

An analytical evaluation of the hybrid boost bearing test rig shown in Figure 13 indicated adequate stress levels for all components and a dramatically modified critical speed map. Where previously a series of criticals existed at the specified test speed range, a single critical speed is now present within the test range and occurs only at a high speed, low axial load condition.

A rotor response calculation was performed at the one critical speed found to exist in the new rig design at the high speed (20,000 rpm) test point in order to assess the effect of operation at or near that speed. The calculated response curve shown in Figure 15 is based on three unbalances located at the fluid film bearing, the spindle rotor midway between the spindle bearings, and at the drive coupling. Two combinations of stiffness and damping coefficient at the damper bearing were also included in the rotor response calculations.

The rotor excursion at the test bearing as shown by Figure 15 is only 20 microinches (0.51×10^{-3} mm) with large amplitudes appearing only at the spindle to gearbox coupling. No adverse effects of the large coupling response is expected since rapid drop off of amplitude occurs on both sides of the peak amplitude curve. Also indicated by Figure 15 is the wide tolerance in both stiffness and damping coefficient the test rig permits at the damper bearing without significant alteration of the response curve.

Based on the favorable results of the analytical study, the test rig components were manufactured and the entire facility assembled for testing. A picture of the test facility and installed rig hardware is provided in Figure 16. The control panel is pictured in Figure 17.

Test Rig Auxiliary Systems

Successful testing of the hybrid boost bearing configuration requires the integration of two major subsystems. These systems have been grouped into the following categories for descriptive purposes.

1. Test Vehicle Drive

The major hardware items which are necessary for testing purposes but which do not contain any hybrid boost bearing components.

2. Fluid Systems

The systems which supply and control the flow of lubricating oil and loading pressures including their monitoring instrumentation required for successful system operation.

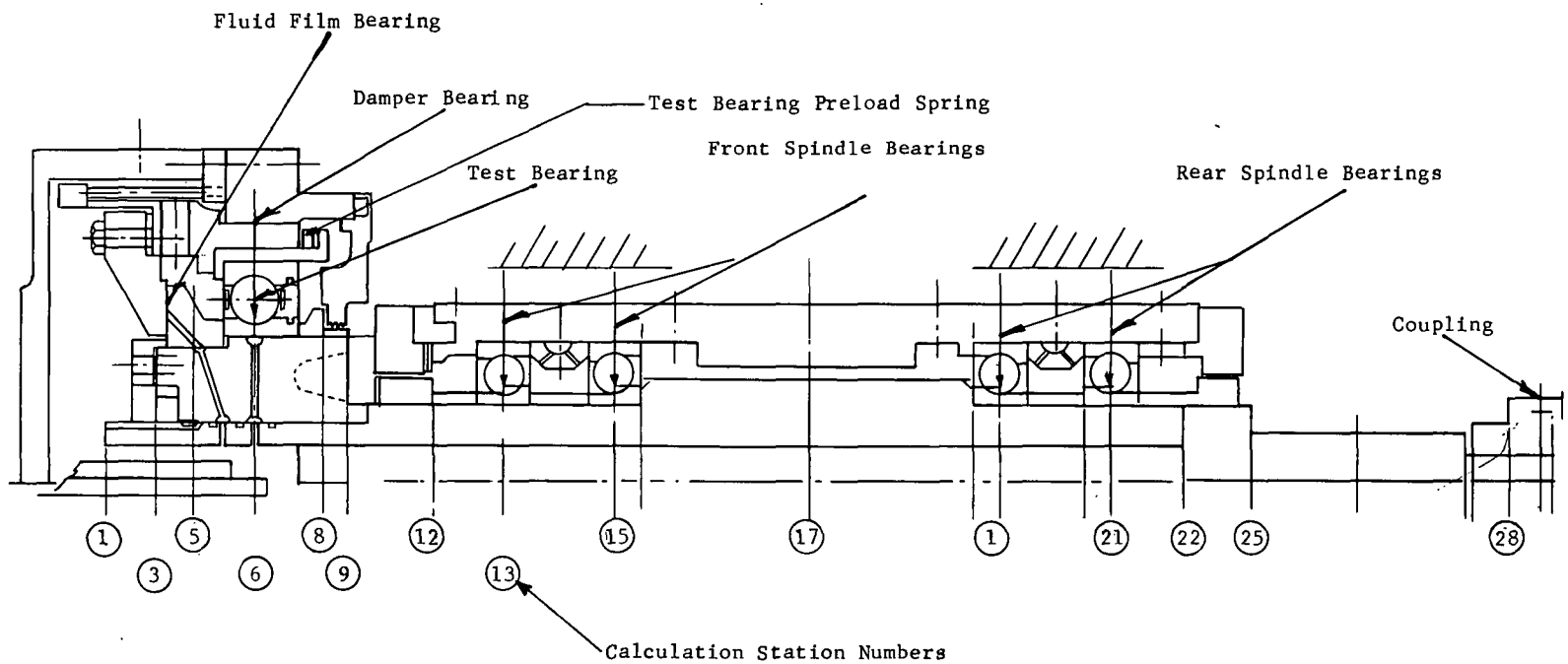

Fig. 13 Hybrid Bearing Test Vehicle

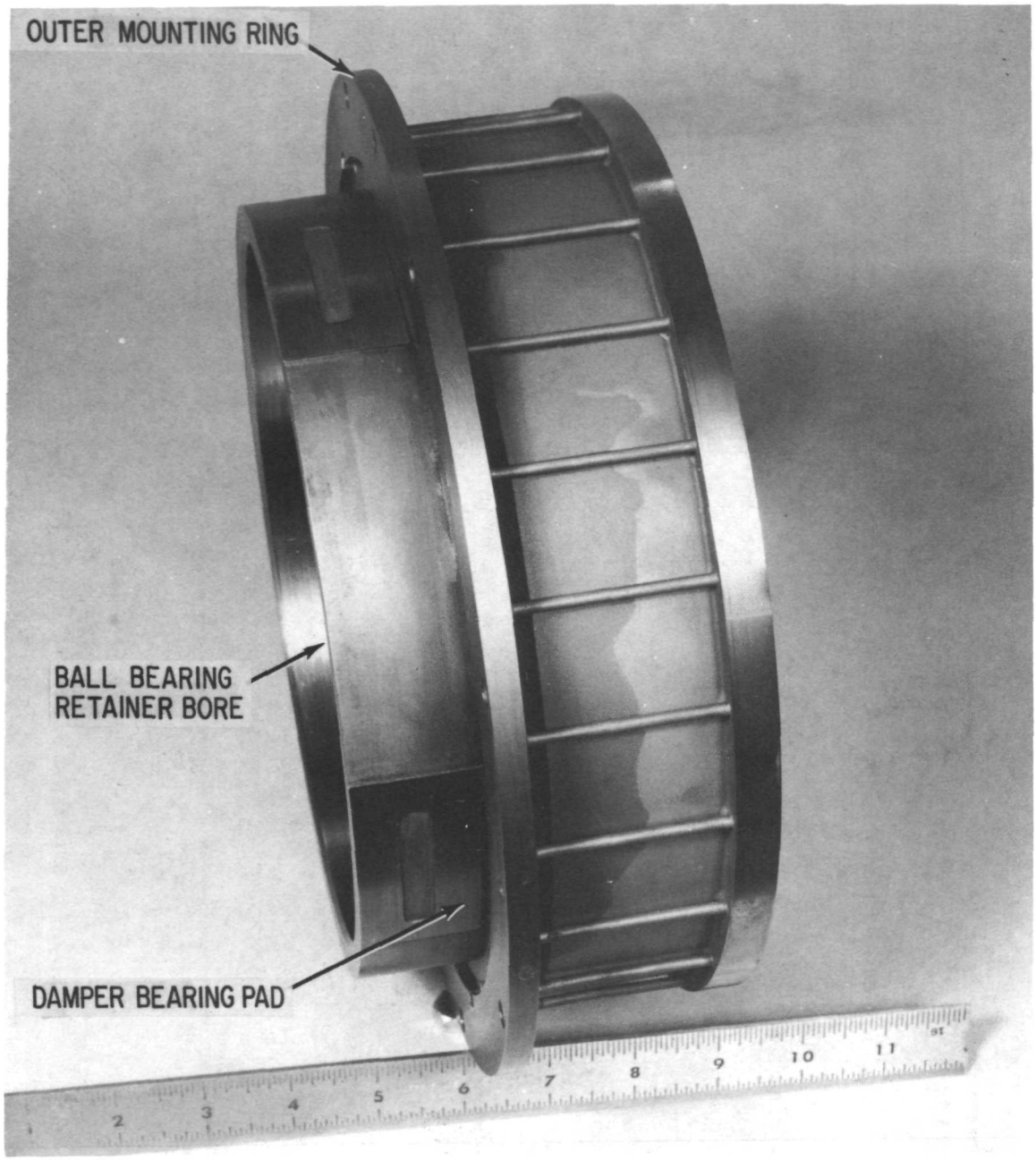

Fig. 14 Hybrid Boost Bearing Cage Assembly

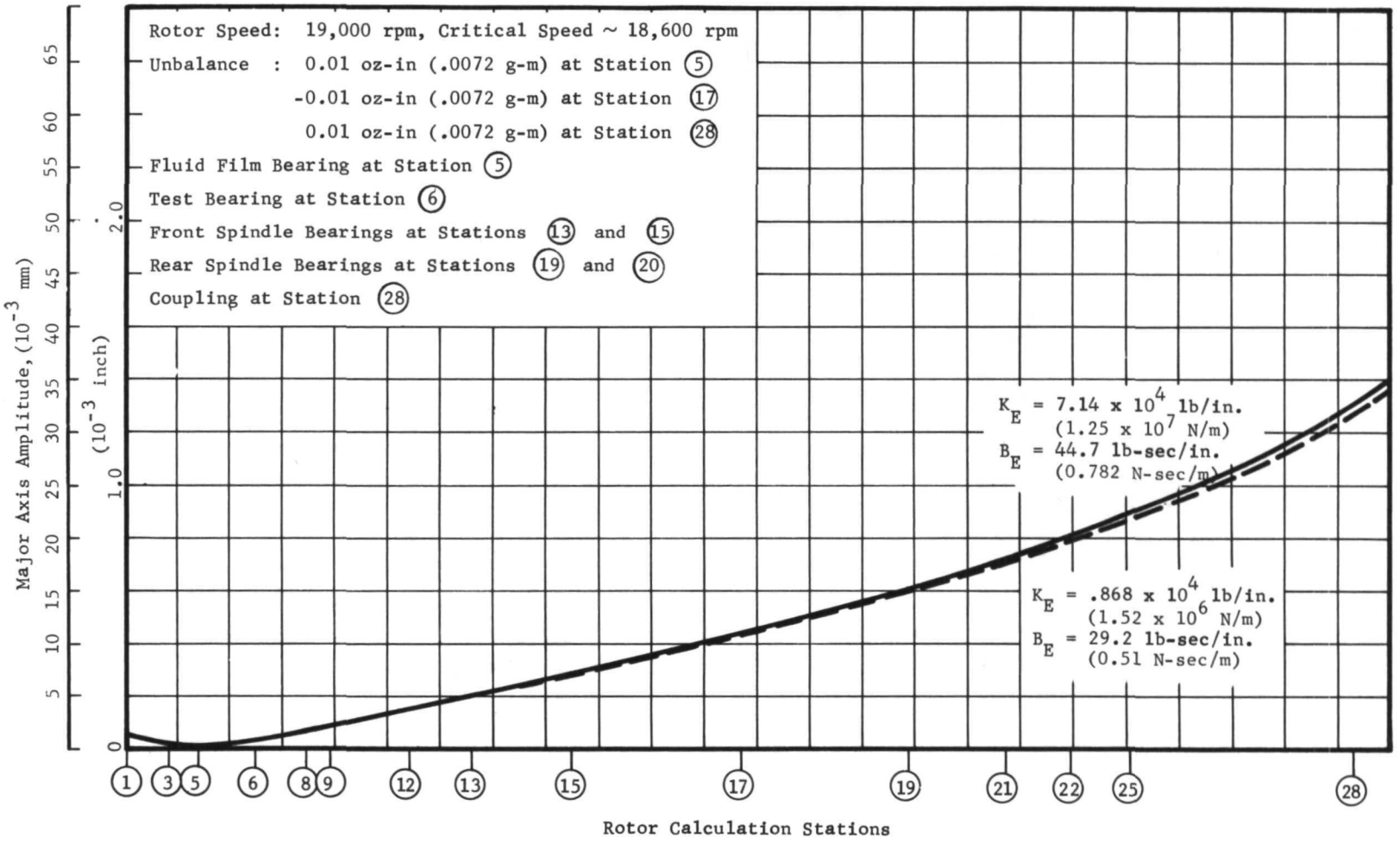

Fig. 15 Rotor Response - Hybrid Bearing Test Rig

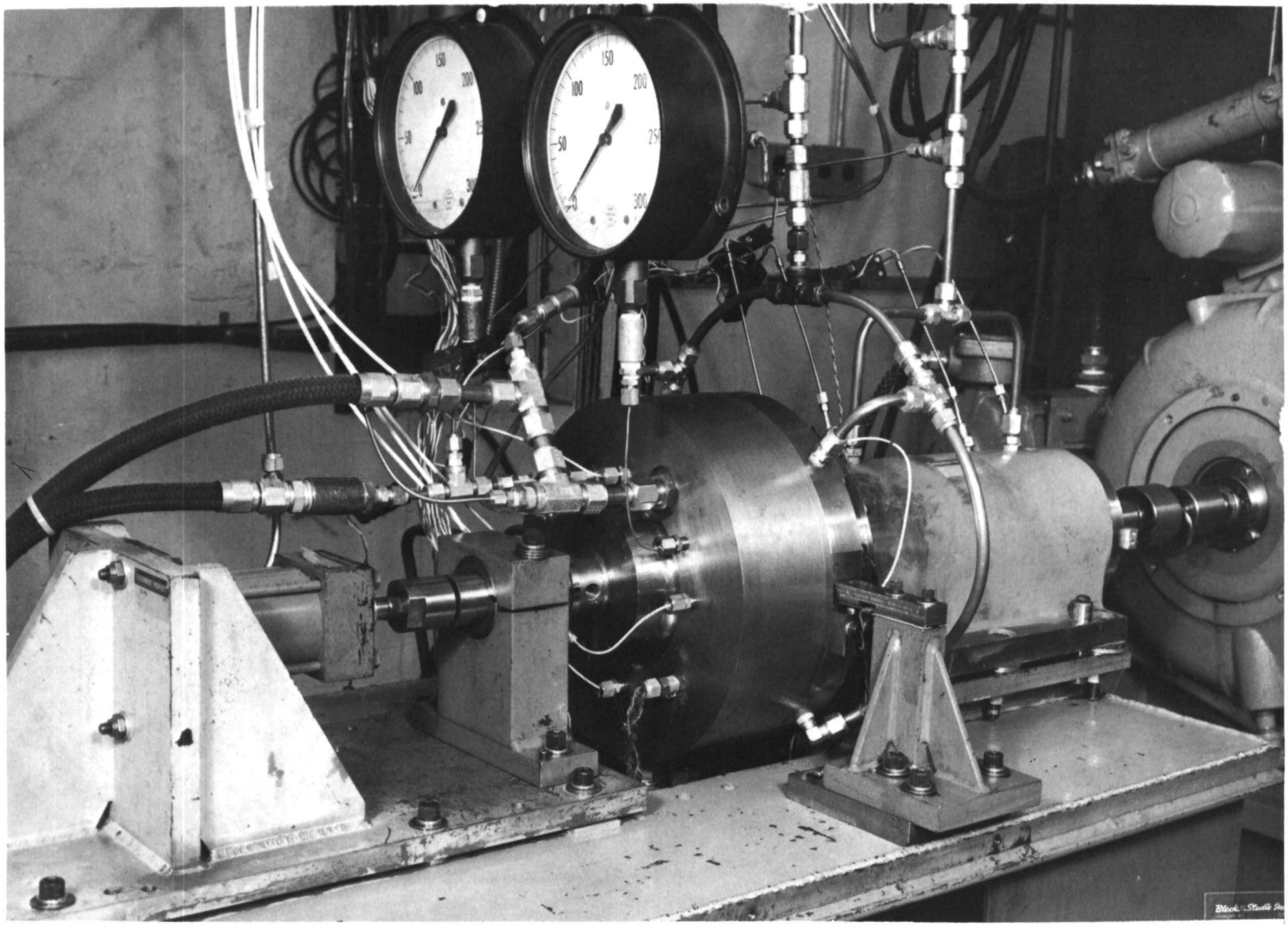

Fig. 16 Hybrid Boost Bearing Test Facility

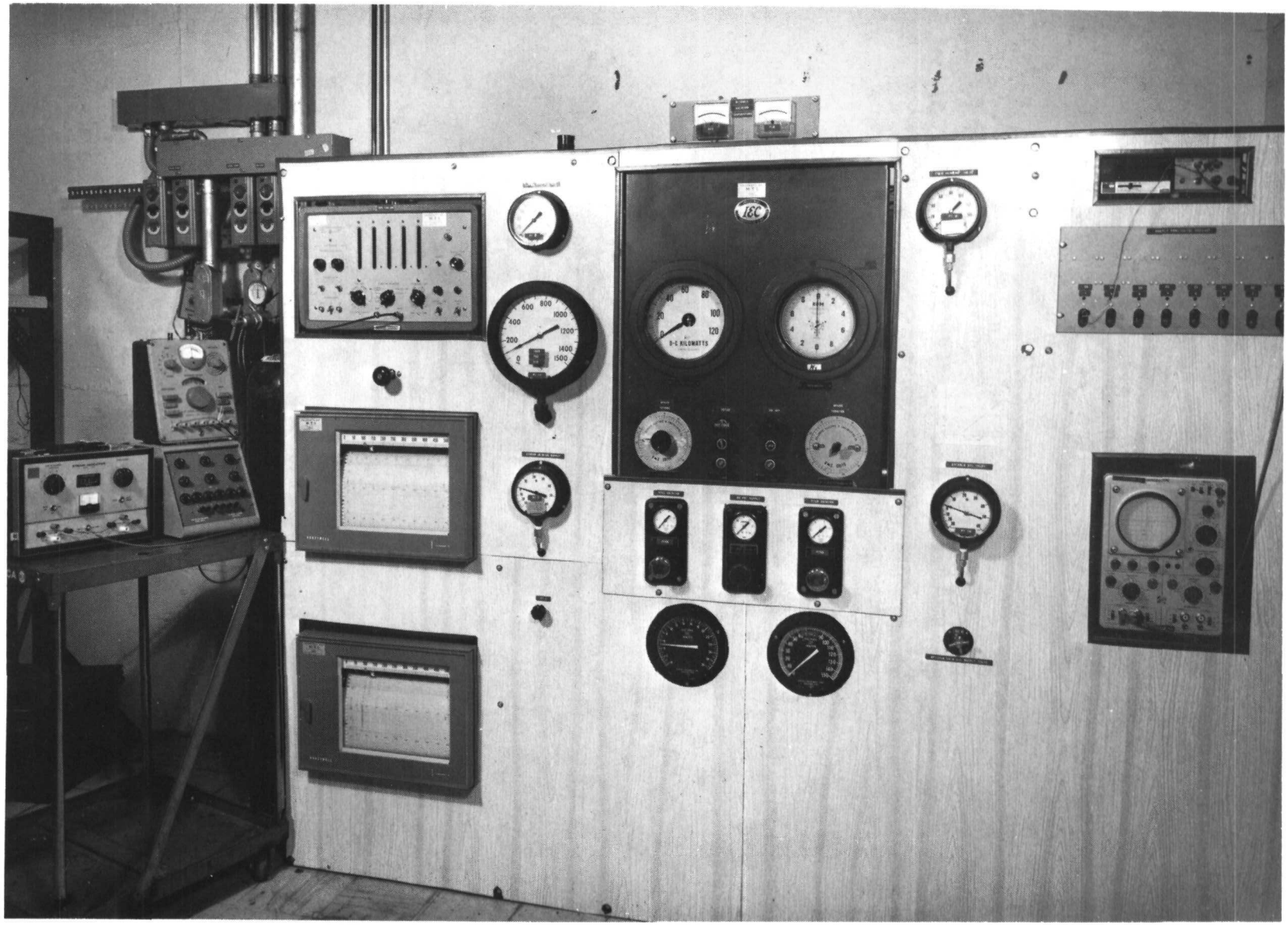

Fig. 17 Hybrid Boost Bearing Test Facility Control Panel

Both the test vehicle drive and fluid system are described in detail in Reference [10].

Test Instrumentation

The test instrumentation shown schematically in Figure 18 was selected to provide accurate measurements of critical hybrid boost bearing performance parameters.

The performance parameters which were instrumented include the following:

1. Speed
2. Power loss (torque)
3. Fluid film and ball bearing temperatures
4. Ball bearing deflection under load
5. Fluid film bearing operating film thickness
6. Fluid film bearing film pressures

Additional performance parameter measurements not indicated in Figure 18 include:

1. Axial load
2. Oil flow rates to the fluid film and ball bearings
3. Oil inlet and scavange temperatures

Specific instrumentation employed to obtain data relevant to the above list is described in the following report sections.

1. Axial Load

Axial load for the hybrid boost bearing is provided by the pneumatic system described in Reference [10]. Measurement of axial load is provided by an accurate pressure gage which indicates the operating pressure of the load cylinder.

Calibration of the complete loading system was performed with the aid of a strain gage load cell of known calibration. At several load settings between 500 (2,229 Newtons) and 5,000 pounds (22,250 Newtons) the pressure at the load cylinder was related to actual load by determining the load cell output. The combined accuracy of the pressure gage and the strain gage load cell results in a load uncertainty of $\pm$ 4.2 pounds (18.7 Newtons) for all tests.

2. Oil Flow Rates to Fluid Film and Ball Bearing

Oil flow rates to both the fluid film bearing and the ball bearing are determined by measuring the pressure drop across the orifice plate flowmeter. Each flow orifice had a sensitive ΔP gage associated with it for calibration purposes. Oil at the specified temperature of 200°F (93.5°C) was pumped through

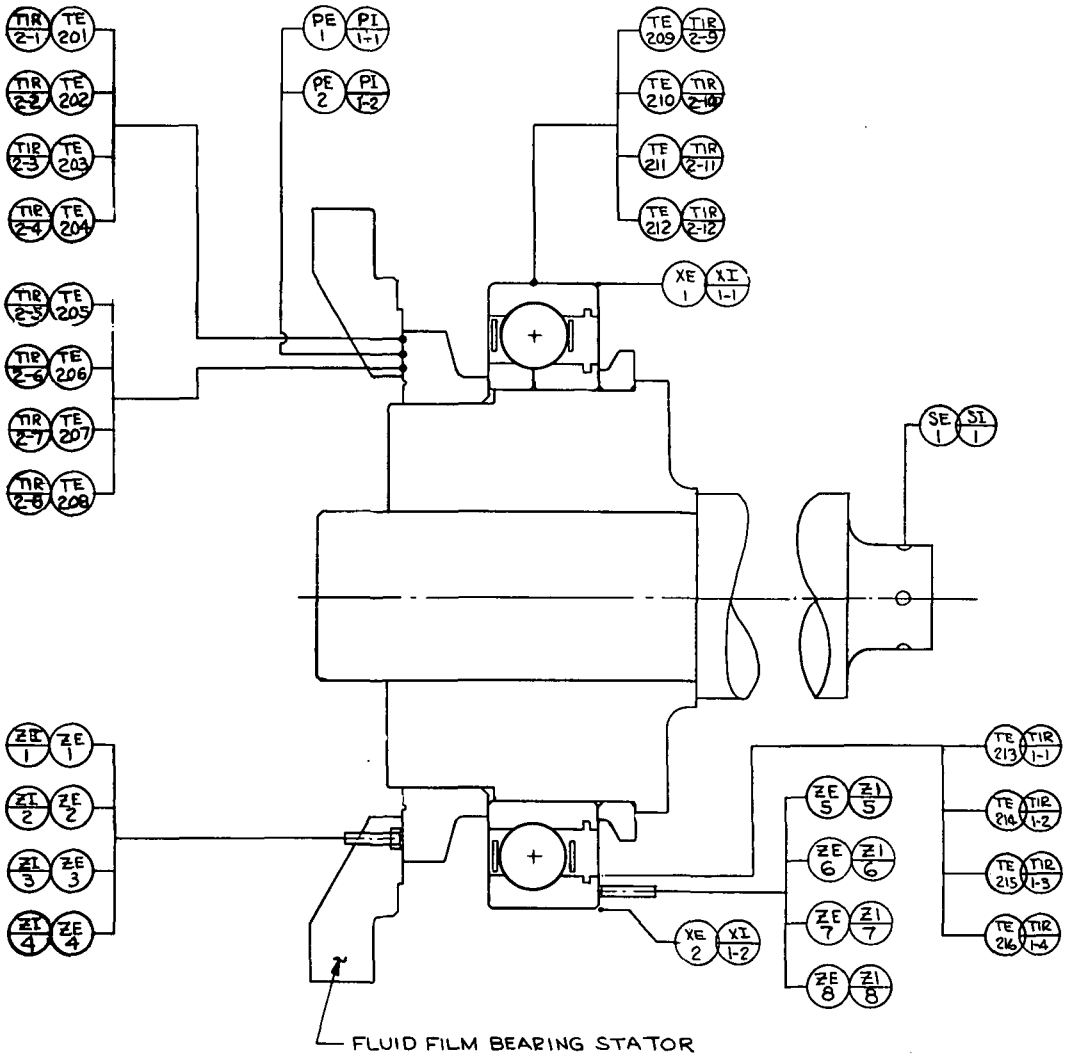

NOTE:
MULTIPLE INSTRUMENT CALLOUTS AT ONE LOCATION INDICATES A CIRCUMFERENTIAL DISPLACEMENT OF 90° BETWEEN SENSORS

PE - PRESSURE SENSOR
PI - PRESSURE INDICATOR
SE - SPEED SENSOR
SI - SPEED INDICATOR
TE - TEMPERATURE SENSOR
TIR - TEMPERATURE INDICATING RECORDER
XE - STRAIN GAGE
XI - STRAIN INDICATOR
ZE - POSITION SENSOR
ZI - POSITION INDICATOR

Fig. 18 Test-Instrumentation Configuration

each flow orifice and was collected in a vessel of known volume. The relationship between the flow passing through the orifice plate and the ΔP across the plate provided a direct measurement of flow rate versus ΔP in the exact test setup, thereby excluding the inaccuracies normally associated with this calibration and resulted in a flow rate accuracy of 3/4 percent of the flow reading at either orifice.

3. Fluid Film Bearing Operating Film Thickness

Four position sensors, identified as ZE-1 through ZE-4 on Figure 18 are permanently mounted in the fluid film bearing stator to provide an accurate measurement of the bearing's operating film thickness. Accurate readability of the position sensors at elevated temperatures in an oil environment is assured with the choice of inductance-type probes.

Four probes were epoxied into the thrust stator and the entire assembly submerged in hot oil for calibration. Precision feeler gage material of known thickness was placed between the thrust stator and the unassembled thrust runner to establish film thickness.

4. Ball Bearing Deflection

The axial deflection of the ball bearing as a function of both load and speed is extremely important in the design and operation of the hybrid boost bearing. The reasons for this are apparent from the previous discussion of the combined performance characteristics of the hybrid boost bearing. To assure proper and accurate measurements of the ball bearing deflection, four proximity probes identified as ZE-5 through ZE-8 on Figure 18 were mounted in the seal plate at the proper radial location to sense motion of the ball bearing outer race relative to the test rig housing. When the preload spring is fully compressed, the relative displacement between the bearing housing and its outer race is equal to zero, and the displacement between the inner and outer races of the ball bearing is equal to that measured between the housing and inner race; i.e., on fluid film bearing probes ZE-1 through ZE-4. On the other hand, when the preload spring is not fully deflected, the true deflection between the inner and outer races of the ball bearing will be equal to the difference between the two measured deflections; those indicated by ZE-1 through ZE-4 and those measured by the seal plate probes ZE-5 through ZE-8.

Calibration of the ball bearing deflection probes (ZE-5 through ZE-8) was performed using the same technique as used with the fluid film probes (ZE-1 through ZE-4). The ball bearing sensor calibrations were performed for six temperatures. These temperatures chosen represent the test temperature of 200°F (93.5°C) and 25°F (13.9°C) increments, both above and below 200°F (93.5°C) for interpolation of position readings for off-design temperature readings. A typical computed probe calibration is shown in Figure 19.

5. Fluid Film Bearing Film Pressures

An additional aid to the evaluation of the hybrid boost bearing is provided by the use of two pressure taps in the fluid film thrust stator. These pressure taps, identified as PE-1 and PE-2 on Figure 18, consist of short lengths of small diameter hypodermic tubing epoxied into the stator. These tubes are

PROBE CALIBRATION
LEAST SQUARE FIT
PN0032
CDC 6600

HYBRID BOOST PROBE CAL
PROXIMETER 1
PROBE ZE1
200 DEGREES F

STATIC CALIBRATION RESULTS .008229 INCHES/VOLT

DISTANCE RELATIVE (INCHES)	DISTANCE MEASURED (MILS)	AMPLITUDE MEASURED (VOLTS)	VARIATION MEASURED-FITTED (VOLTS)	VARIATION MEASURED-FITTED (INCHES)
0.000000	0.000000	2.640	.01973	-.000162
.002500	2.500000	2.915	-.00907	.000075
.004000	4.000000	3.095	-.01135	.000093
.006000	6.000000	3.350	.00062	-.000005
.008000	8.000000	3.595	.00258	-.000021

DISTANCE RELATIVE (INCHES)	DISTANCE MEASURED (MILS)	AMPLITUDE MEASURED (VOLTS)	VARIATION MEASURED-FITTED (VOLTS)	VARIATION MEASURED-FITTED (INCHES)
0.000000	0.000000	2.625	.00473	-.000039
.002500	2.500000	2.910	-.01407	.000116
.004000	4.000000	3.095	-.01135	.000093
.006000	6.000000	3.360	.01062	-.000087
.008000	8.000000	3.600	.00758	-.000062

CALIBRATION RESULTS .008219 INCHES/VOLT
VARIATION + OR - .000609

EQUATION OF CURVE

X = DISTANCE
Y = VOLTAGE

X = -.027634 + .012178 Y + -.000634 Y**2

DISTANCE (INCHES)	AMPLITUDE (VOLTS)	SLOPE (INCHES/VOLT)	SLOPE NORMALIZED
0.000000	2.625	.008847	1.076429
.002500	2.910	.008485	1.032464
.004000	3.095	.008250	1.003860
.006000	3.360	.007914	.962944
.008000	3.600	.007609	.925887

Fig. 19 Computed Probe Calibration

lapped flat to the thrust surface and communicate with the annular recess of the thrust runner.

Film pressure transmitted by the tubing is sensed and indicated by two pressure gages (PI-1 and PI-2). Both gages were calibrated against a master gage and were found accurate to within one psi.

6. Power Loss (Torque)

Power loss (torque) was measured through the use of strain gage torque arms built into the floating bearing housing. The torque arm arrangement is detailed in Reference [10]. The two torque arms which are attached to the test rig housing contain balls which transmit the torque load to a point contact onto deflection beams that are instrumented with strain gages. These beams are allowed to deflect a limited amount before they engage solid stops.

7. Rotational Speed

Shaft rotational speed is indicated by a digital pulse counter (SI-1 on Figure 18). Input to the counter is provided by a magnetic pickup (SE-1 on Figure 18) located at the drive end of the high-speed spindle. Six surface discontinuities on the spindle shaft permit speed readings to the nearest 10 rpm $\pm$ 1 count.

8. Test Temperatures

Test rig temperature measurements were obtained with Iron-Constantan thermocouples. Thermocouple outputs were printed out on multipoint recorders identified as TIR-1 and TIR-2 on Figure 18 and were accurate to 4 $\pm$ 1°F (2.22 $\pm$ .56°C). Individual thermocouples identified by 200 series TE numbers were placed in the positions as designated in Table 8.

EXPERIMENTAL RESULTS

The design concepts, final hardware configuration, auxiliary support systems, and test instrumentation for the parallel hybrid bearing test program have all been described in previous sections of this report. The following report sections will describe the experiments conducted to evaluate the parallel hybrid bearing configuration and discuss the experimental results.

Three interrelated tests were attempted within the experimental program; these were:

1. Evaluation of the test ball bearing
2. Evaluation of the fluid film bearing
3. Evaluation of the combined ball bearing fluid film bearing in the parallel hybrid bearing configuration

Each of the above tests followed a test sequence listed in Table 9, with these

TABLE 8

TEST THERMOCOUPLE LOCATION IDENTIFICATION

POSITION	IDENTIFICATION
Fluid Film Bearing Stator Temperature Outer Radius - 0^{o}	TE-201
Fluid Film Bearing Stator Temperature Outer Radius - 90^{o}	TE-202
Fluid Film Bearing Stator Temperature Outer Radius - 180^{o}	TE-203
Fluid Film Bearing Stator Temperature Outer Radius - 270^{o}	TE-204
Fluid Film Bearing Stator Temperature Inner Radius - 0^{o}	TE-205
Fluid Film Bearing Stator Temperature Inner Radius - 90^{o}	TE-206
Fluid Film Bearing Stator Temperature Inner Radius - 180^{o}	TE-207
Fluid Film Bearing Stator Temperature Inner Radius - 270^{o}	TE-208
Test Bearing Outer Race Temperature at 0^{o}	TE-209
Test Bearing Outer Race Temperature at 90^{o}	TE-210
Test Bearing Outer Race Temperature at 180^{o}	TE-211
Test Bearing Outer Race Temperature at 270^{o}	TE-212
Ball Bearing Position Sensor Temperature 0^{o}	TE-213
Ball Bearing Position Sensor Temperature 90^{o}	TE-214
Ball Bearing Position Sensor Temperature 180^{o}	TE-215
Ball Bearing Position Sensor Temperature 270^{o}	TE-216

Additional IC thermocouples, not identified on Figure 18, were placed to measure fluid film bearing oil inlet temperature, ball bearing oil inlet temperature and scavenge temperatures.

TABLE 9

TEST SEQUENCE: HYBRID BOOST BEARING EVALUATION

1.0 Rotational speed = 0 rpm

1.1 Adjust flow rates to give:

1 gpm at ball bearing

4 gpm at spindle

Oil flow at fluid film bearing as required, but not to exceed 7 gpm

1.1.1 Thrust load = 500 lbs. (2224 Newtons)

1.1.2 Thrust load = 1,000 lbs. (4448 Newtons)

1.1.3 Thrust load = 3,000 lbs. (13344 Newtons)

1.1.4 Thrust load = 5,000 lbs. (22,240 Newtons)

2.0 Rotational speed = 10,000 rpm - repeat 1.1, except for 1.1.1, 500 lbs. thrust load.

3.0 Rotational speed = 15,000 rpm = repeat 1.1, except for 1.1.1, 500 lbs. thrust load.

4.0 Rotational speed = 20,000 rpm - repeat 1.1 except for 1.1.1, 500 lbs. thrust load.

exceptions:

1. Both fluid film and full parallel hybrid bearing tests did not include a zero rpm run.
2. Both fluid film and full parallel hybrid bearing tests required a variation in the fluid film bearing flow rates which resulted in some instances in flow rate demands exceeding system capacity.

A description of the test results for each of the three bearing tests is given in the following subsections.

Ball Bearing Tests

The ball bearing represents an important component of the hybrid boost bearing system and the knowledge of its operational characteristics is necessary for the satisfactory implementation of the hybrid boost principle. To satisfy this necessity, two tests involving only the ball bearing were performed concurrently; these tests are identified as follows:

1. Load-deflection characteristics tests - Where the relative displacement of the ball bearing races is measured as a function of both speed and load.
2. General bearing performance tests - Where performance parameters such as temperature rise and power loss are determined.

A discussion of the results of the above tests is presented below.

1. Load-Deflection Characteristics - Ball Bearing

The load deflection characteristics (or axial stiffness) of the ball bearing must be established to determine the hybrid boost bearing performance. The load sharing between the fluid film and ball bearing components of the hybrid boost bearing, as well as any fail-safe feature are both dependent upon a firm knowledge of these characteristics. The axial load versus deflection test data taken at different speeds for the 125 mm ball bearing selected for this series of tests are given in Table 10. The given deflection is measured in terms of the clearance present between the runner and stator of the fluid film bearing. The change in clearance represents the actual deflection of the ball bearing since the preload spring system is fully compressed at and above the 1,000 pound (4,448 Newton) load condition. For presentation purposes, deflection data is referenced to a zero base representing the position at an axial bearing load of 5,000 pounds (22,240 Newtons) and zero speed. A comparison between test values of the actual bearing deflection with calculated results relative to each speed (10,000, 15,000, and 20,000 rpm) tested is shown in Figure 20. The agreement between calculated values and the actual test values is very good at 10,000 and 15,000 rpm. At 20,000 rpm, while the slope of the curve (i.e., stiffness) is in reasonable agreement, the curve appears to be displaced by 2.15 mils (0.055 mm) at 1,000 pounds (4,448 Newtons) and by 1.6 mils (0.0345 mm) at 5,000 pounds (22,240 Newtons) of axial load.

The theoretical values computed on RECAP* have been compensated for in centrifugal

* Rolling Element Computer Analysis Program

TABLE 10

TEST BALL BEARING EXPERIMENTAL
LOAD-DEFLECTION TEST RESULTS

T_{in} = 200°F (93.5°C) Q = 1.0 gpm (0.63×10^{-4} m^3/sec)

Speed, rpm	Axial Load lbs.	Axial Load Newtons	Deflections inch	Deflections mm	Average Stiffness lb/in	Average Stiffness Newton/meter
0	5000	(22,240)	0	0		
10,000	1000	(4448)	3.62×10^{-3}	(0.092)	$.99 \times 10^{6}$	(1.73×10^{8})
	3000	(13,344)	1.6×10^{-3}	(0.046)	2.00×10^{6}	(3.5×10^{8})
	5000	(22,240)	0.6×10^{-3}	(0.015)		
15,000	1000	(4448)	5.2×10^{-3}	(0.132)	1.43×10^{6}	(2.52×10^{8})
	3000	(13,344)	2.8×10^{-3}	(0.071)	1.25×10^{6}	(2.19×10^{8})
	5000	(22,240)	1.2×10^{-3}	(0.032)		
20,000	1000	(4448)	7.62×10^{-3}	(0.194)	1.33×10^{6}	(2.32×10^{8})
	3000	(13,344)	5.92×10^{-3}	(0.150)	1.05×10^{6}	(1.84×10^{8})
	5000	(22,240)	4.02×10^{-3}	(0.102)		

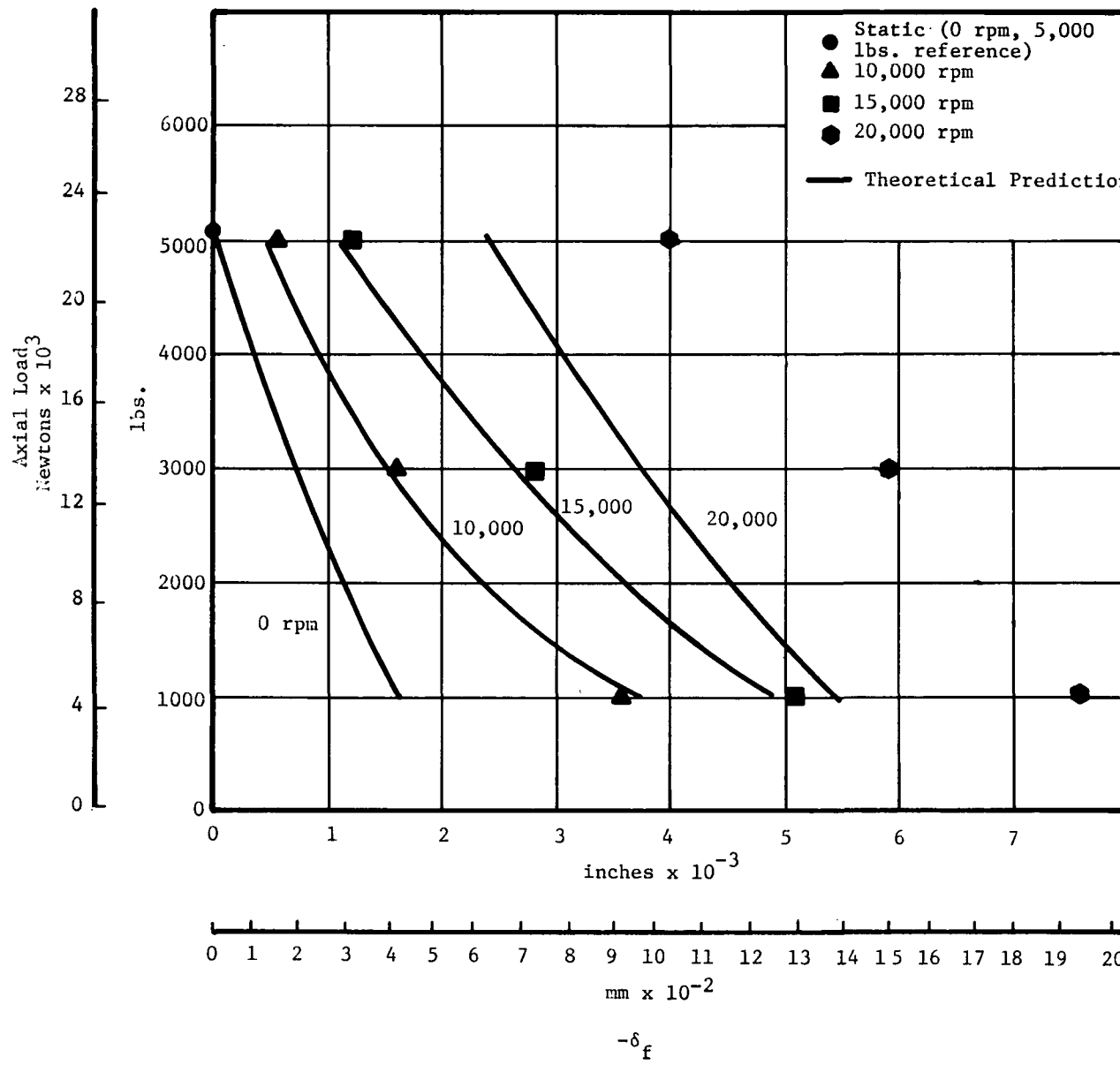

Fig. 20 Comparison Between Theoretical and Test Results for Test Ball Bearing

growth as discussed in the section on ball bearing analysis. The differences observed at the 20,000 rpm speed (assuming that the inductance probe readings are correct) should mainly be due to differential thermal expansion within the ball bearing.

To check on this hypothesis as a first approximation one may assume that the balls operate at the same temperature as the inner race. Let us further assume that this temperature is 40°F higher than the outer race temperature. The decrease in internal clearance is

$$\Delta P_d = \alpha D \, \Delta T \tag{13}$$

where

α = 6.72×10^{-6} in/in/°F (12.1×10^{-6} mm/mm/°C)

D = 7.0 inches (179 mm)

ΔT = 40°F (22.2°C)

Substituting these values in Equation (13) $\Delta P_d = 1.88$ (10^{-3}) inches (.0135 mm).

Knowing ΔP_d one can calculate the effect of this change in internal clearance on the contact angle from [14],

$$\cos \beta' = \frac{2BD_w - P_D + \Delta P_D}{2BD_w} \tag{14}$$

where

$B = f_o + f_i - 1 = .04$

f_o, f_i = outer and inner race curvature ratios

D_w = ball diameter = .8125 inches (20.6 mm)

P_D = initial internal clearance = 11.42×10^{-3} inches (.290 mm) at a contact angle of 20.58° corresponding to the initial contact angle at 10,000 rpm

$\cos\beta'$ = new mounted contact angle

Using the above specified values and solving for angle β', $\beta' = 15.67°$. To determine the effect of the new contact angle on the initial axial reference position

$$P'_E = 2 BD_w \sin\beta'$$

$P'_E = 17.6 \times 10^{-3}$ inches (0.448 mm)

The initial axial play corresponding to the mounted* contact angle of 20.58° is equal to 22.84 mils (0.580 mm). The difference in the axial play between the initially "mounted" bearing without thermal gradients and that with a thermal gradient of 40°F is 5.24 mils (0.132 mm) of which only one half [i.e., 2.62 mils (0.066 mm] will act to offset the measured clearance. Hence, a thermal gradient of 40°F can more than compensate for the recorded differences between the measured and calculated load versus deflection values at 20,000 rpm.

2. Test Ball Bearing - Performance Tests

Additional ball bearing performance data was obtained in conjunction with the collection of load-deflection data. This data is listed in Table 11 to indicate the agreement achieved. The theoretical power loss was obtained from Reference [15],

$$q = 3.19\ (10^{-8})(dN)^{1.5}\ W^{0.07}\ \mu^{0.25}\ m^{0.42}$$

where q is the bearing heat rejection in Btu/min, μ is oil viscosity in cps, d is bearing bore diameter in mm, N is speed in rpm, F_a is axial load in pounds, and m is oil flow in lb/sec. Converting this equation to horsepower,

$$HP = 7.52\ (10^{-10})\ (dN)^{1.5}\ W^{0.07}\ \mu^{0.25}\ m^{0.42}$$

Since a lubricant film in the fluid film bearing was maintained to provide an oil bath at the position sensors to duplicate the calibration conditions, significant losses sufficient to mask the bearing losses were induced at high load levels. The difference in power loss at 20,000 rpm can also in a large measure be attributed to oil churning losses within the bearing sump induced at this speed.

The ball bearing outer race temperatures shown in Table 11 are very similar to those reported upon in Reference [16] at similar conditions of operation.

Based on the above results it can be concluded that:

1. The slope of this test ball bearing load-deflection curve; i.e., its stiffness characteristic, has been verified experimentally and is in good agreement with predicted values.
2. Relative bearing race displacement as a function of inner race rotational speed is significantly affected by centrifugal and differential thermal growth effects on the inner race.

Fluid Film Bearing Tests

The centrifugally-fed fluid film bearing test data was obtained with the

* The mounted contact angle takes into account the centrifugal growth effect on the internal bearing clearance, as well as that of the interference fit.

TABLE 11

TEST BALL BEARING EXPERIMENTAL PERFORMANCE DATA

Speed rpm	DN	Load lb (N)	T_i °F (°C)	T_o °F (°C)	$T_{outer\ race}$ °F (°C)	Q gpm (m^3/sec)	Power HP exp.	Calculated Power HP
10,000	1.25×10^6	1000 (4448)	201 (94.0)	250 (121)	228 (110)	1.03 (0.66×10^{-4})	5.9	5.4
		3000 (13344)	202 (94.5)		235 (113)	1.03 (0.66×10^{-4})		
		5000 (22240)	201 (94.0)		242 (116)	1.03 (0.66×10^{-4})		
15,000	1.88×10^6	1000 (4448)	199 (93.5)	286 (141)	256 (124)	1.03 (0.66×10^{-4})	9.8	10.0
		3000 (13344)	200 (93.6)		268 (131)	1.03 (0.66×10^{-4})		
		5000 (22240)	200 (93.6)		279 (137)	1.03 (0.66×10^{-4})		
20,000	2.5×10^6	1000 (4448)	194 (90.0)	330 (165)	273 (134)	1.03 (0.66×10^{-4})	24.0	15.5
		3000 (13344)	190 (88.0)		285 (140)	1.03 (0.66×10^{-4})		
		5000 (22240)	203 (95.2)		310 (154)	1.03 (0.66×10^{-4})		

objective of determining the fluid film bearings operating characteristics over a range of film thicknesses and loads. The fluid film bearing tests were conducted for a test head setup which provided for preload only on the ball bearing. To bring about the proper load distribution, sufficient material was removed from the bearing spacer to produce a 750 pound (3,360 Newton) ball bearing preload at zero speed. Under this setup arrangement the preload spring was always active and at any load condition the preload spring load-deflection characteristic was utilized to correct for changes in preload due to changes in the fluid film bearing film thickness. Subtracting the corrected preload from the known externally-applied axial load provided the fluid film bearing load. In addition to the above method of determining fluid film bearing load capacity, a direct measure of feed slot pressure was obtained via the pressure taps previously identified. The product of the measured feed slot pressure and the effective bearing area (5.346 in^2) provides the second measure of fluid film bearing load capacity.

Because the lubricant was supplied by injection into a rotating shaft, the procedure used in determining a flow rate which matched the flow requirement of the fluid film bearing was for the test operator to slowly increase the lubricant supply to the bearing while monitoring the feed groove pressure. The flow rate at which the film pressure failed to increase further was considered as the condition of satisfied flow. Reduction in clearance through increase in loading normally requires lower flows. Since the flow rate was set at the large clearances, at low clearances the excess flow automatically discharged into the sump.

A test sequence as outlined in Table 9 was performed with the above-described setup. These data are presented in Table 12 with the load deflection data plotted in Figures 21, 22, and 23 for 10,000, 15,000, and 20,000 rpm respectively. It is evident from Figure 21 that good agreement between the experimental and theoretical bearing performance at 10,000 rpm was obtained. Significant divergence, however, from theoretical predictions at high test speeds is shown in Figures 22 and 23.

As was previously mentioned, the load acting on the fluid film bearing was determined by virtue of a direct (actual measurements of applied load minus preload) and indirect (pressure multiplied by effective area) method. The results of the two methods are shown in Table 12, columns 2 and 4. A direct comparison is also given in Figures 21 through 23.

Agreement between the two load measurement techniques indicates the acceptability of determining fluid film load capacity by means of feed-slot pressure. A loss of accuracy from this measurement technique, however, occurs at speeds of 15,000 and 20,000 rpm. This may be due to pressure profile distortions.

The lower than expected load-carrying capacities at 15,000 and 20,000 rpm are at a first glance puzzling, however, a close examination of the data does indicate that the lack of performance at high speeds is probably due to thermo-elastic deformations of the fluid film bearing.

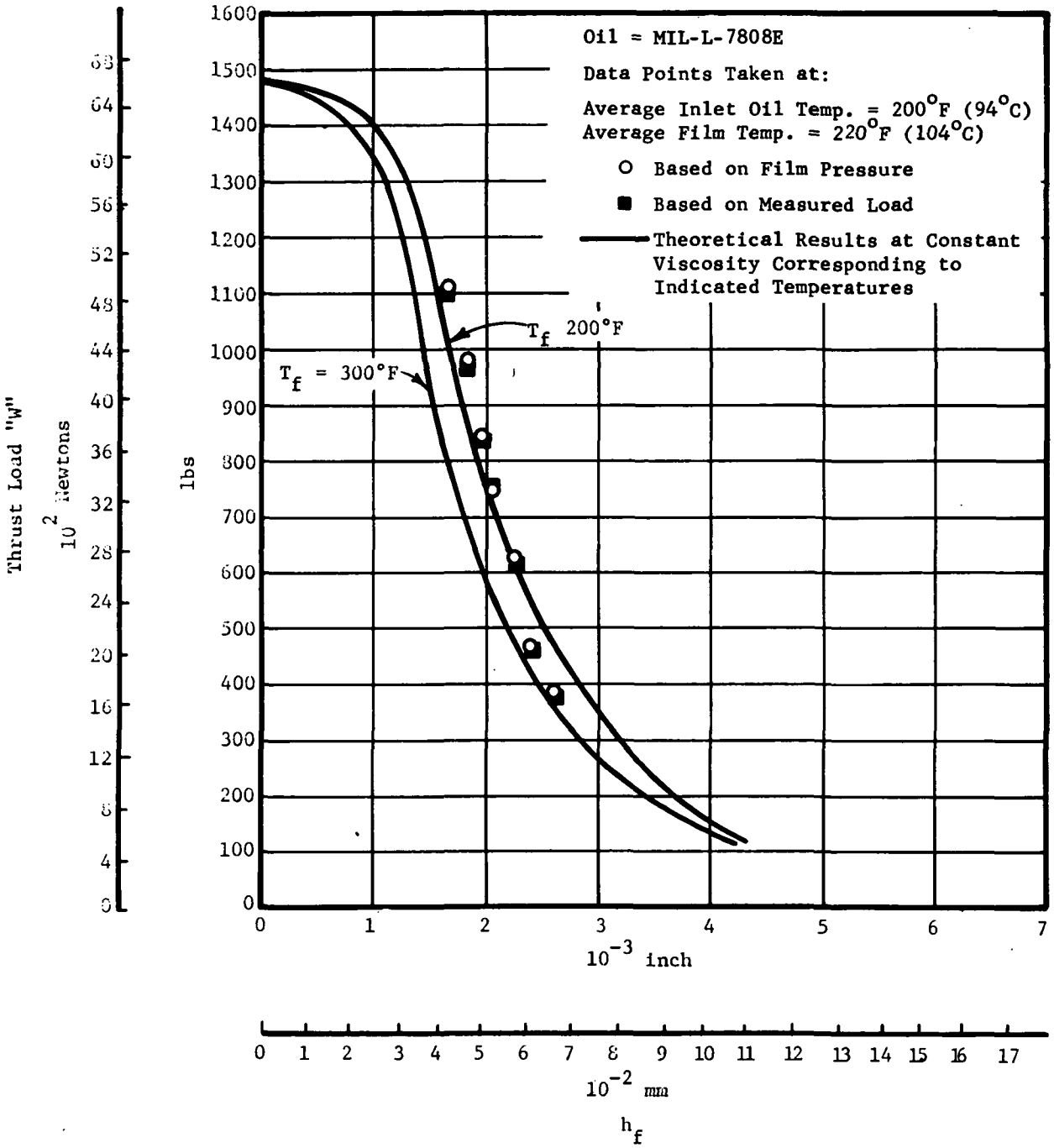

Fig. 21 Fluid Film Bearing Performance
N = 10,000 rpm

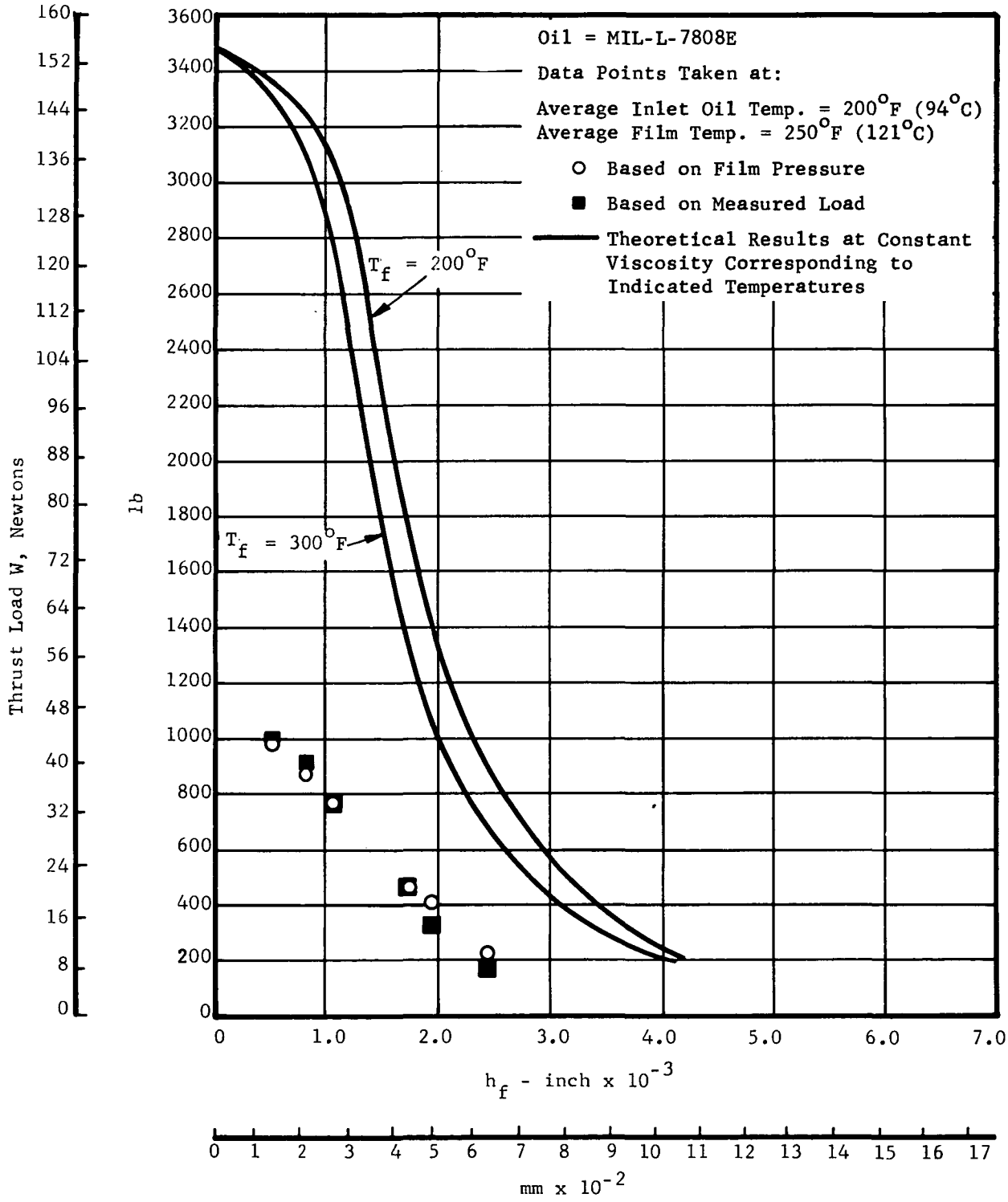

Fig. 22 Fluid Film Bearing Performance
N = 15,000 rpm

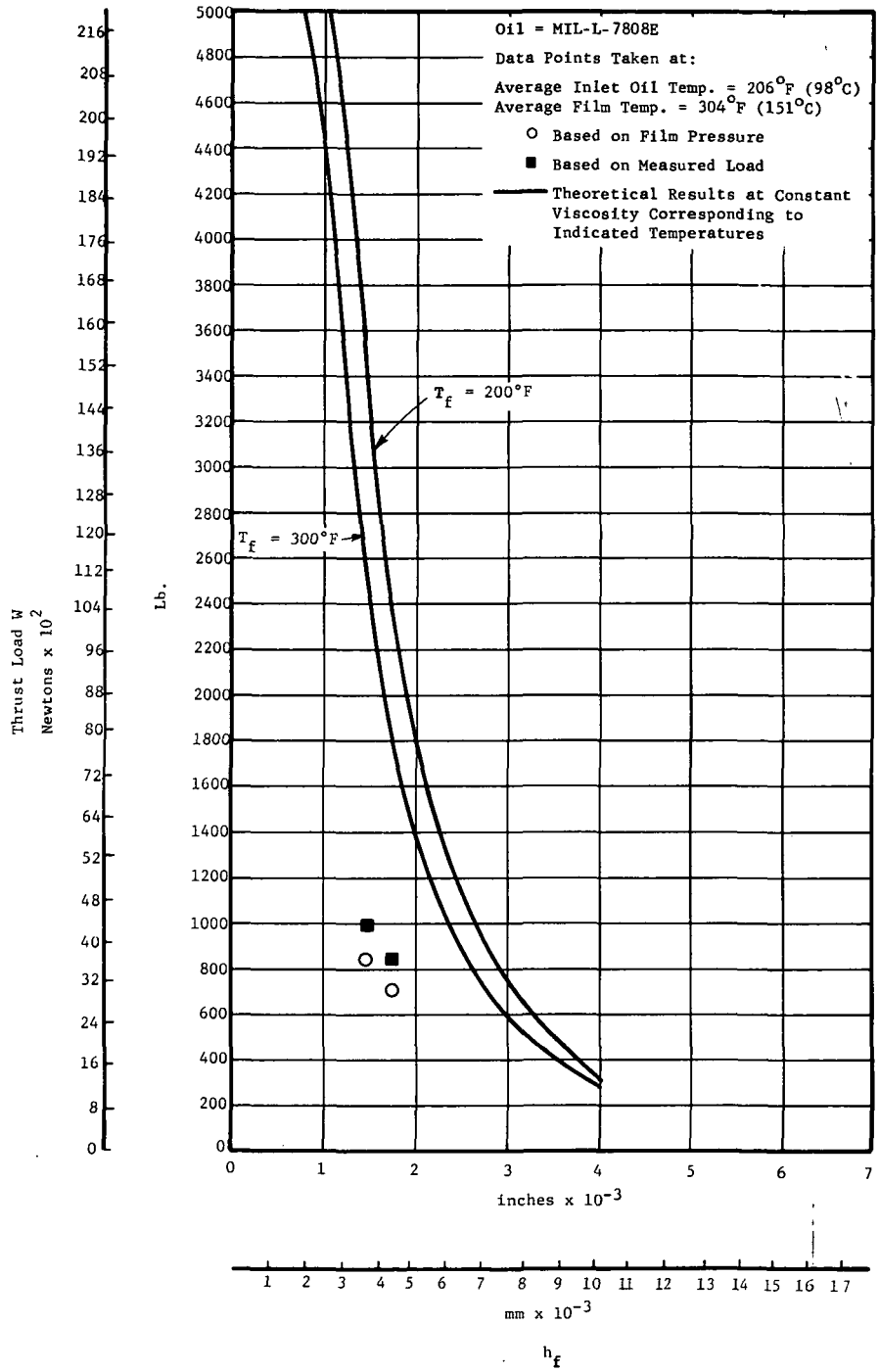

Fig. 23 Fluid-Film Bearing Performance - 20,000 rpm

The presence of thermo-elastic deformations in the bearing can be deduced from the measured temperatures of the bearing stator face which do, to a large extent, also reflect the face temperatures of the rotor face. High temperatures at the bearing faces, in turn, point to the existence of high, axial thermal gradients which will result in a distorted oil film that diverges at the outside and converges at the inside diameter of the fluid film bearing. This type of distortion brings about a lower flow requirement at a reduced load carrying capacity (Reference 17).

The data shown in Table 12 reveals the existence of stator face temperatures which are appreciably higher than those of the oil into the bearing. Note that the first test point at 15,000 rpm produced 260°F face temperatures, while in the 20,000 rpm run temperatures as high as 300°F were recorded. This will invariably result in an oil film distortion similar to the one described above.

Throughout the test sequence the results of which are listed in Table 12, the inner land temperatures were higher than those of the outer land. Small temperature differences can be attributed to the thermal distortions in the oil film. In some instances, however, the inner land temperatures were appreciably higher than those of the outer land. At those conditions only substantial increases in the bearing pressure produced by an increase in the externally applied load and corresponding decrease in the operating film thickness, brought about a drastic reduction in thermal differential between outer and inner land temperatures. This phenomenon can be attributed to the centrifugal effects in the oil film. At high speeds and large film thickness the bearing pressure is low, and the centrifugal pressure buildup in the film can approach the magnitude of the downstream pressure at the bearing orifices. Correspondingly the flow and heat removal through the inner land will decrease, bringing about a rise in inner land temperatures. At the same time, the increase in centrifugal effects at the outer land increases the flow resulting in more efficient heat removal and lower outer land temperatures. This further increases the degree of thermal deformation of the bearing faces and results in lower load carrying capacity.

In summary, the fluid film bearing showed limited success. Predictable performance was exhibited at the lower test speeds with divergence between analytical and experimental performance increasing with increasing speed. The combination of thermally distorted bearing faces and centrifugal pressure effects in the oil film is viewed as being the primary cause effecting this divergence.

Hybrid Boost Bearing Tests

The hybrid boost bearing test configuration utilizes the combined load-carrying capability of both the ball bearing and the hydrostatic fluid film bearing to

TABLE 12

FLUID FILM BEARING PERFORMANCE

Speed rpm	Net External Load lb. (Newton)	Film Thickness 10^{-3} Inch (mm)	Film Pressure Load psi/lb ($N/m^2/N$)	Inlet Oil Temp. °F (°C)	Average Film Temp. °F (°C)	Radial+ ΔT °F (°C)	Power Loss hp	Q_3 gpm (m^3/sec)
10,000	378 (1680)	2.59 (0.066)	72.5/384 (50 x 10^4/1710)	198 (92.2)	220 (104)	1 (0.55)	6.6	4.85 (3.06 x 10^{-4})
	461 (2040)	2.39 (0.061)	87.0/461 (60 x 10^4/2050)	204 (95.5)	228 (109)	2 (1.11)	7.1	
	607 (2690)	2.25 (0.057)	117.5/623 (81 x 10^4/2770)	200 (93.5)	220 (104)	0 (0)	7.6	
	732 (3250)	2.09 (0.053)	140.5/745 (97 x 10^4/3320)	205 (96.2)	225 (107)	2 (1.11)	8.2	
	836 (3700)	1.95 (0.050)	160.0/848 (110 x 10^4/3760)	204 (95.6)	224 (106)	0 (0)	8.6	
	961 (4260)	1.83 (0.047)	186.0/986 (128 x 10^4/4380)	199 (93.0)	221 (105)	2 (1.11)	9.2	
	1100 (4900)	1.67 (0.043)	209.5/1110 (144 x 10^4/4950)	197 (91.8)	222 (106)	6 (3.33)	9.6	
15,000	170 (760)	2.44 (0.062)	42.5/225 (29 x 10^4/1000)	199 (93.0)	260 (126)	31* (17.2)	19.0	5.7 (3.59 x 10^{-4})
	336 (1490)	1.99 (0.050)	76.0/403 (52 x 10^4/1790)	193 (89.5)	249 (120)	26* (14.4)	27.4	
	474 (2120)	1.75 (0.044)	87.5/464 (60 x 10^4/2060)	203 (94.7)	251 (122)	14* (7.76)	28.8	
	753 (3350)	1.05 (0.025)	143.5/761 (99 x 10^4/3380)	200 (93.5)	242 (117)	5 (2.77)	29.	
	920 (4070)	.78 (0.020)	166.0/880 (115 x 10^4/3900)	197 (91.8)	238 (114)	1 (0.55)	29.3	
	1036 (4600)	.54 (0.014)	183.5/973 (127 x 10^4/4320)	195 (90.2)	237 (114)	2 (1.11)	30.2	
20,000	857 (3820)	1.73 (0.044)	133.0/705 (92 x 10^4/3130)	206 (96.5)	300 (148)	47* (26)	65.8	6.5 (4.1 x 10^{-4})
	1003 (4450)	1.45 (0.037)	158.5/840 (109 x 10^4/3730)	205 (96.2)	307 (153)	42* (23.3)	--	5.8 (3.65 x 10^{-4})

+ Positive ΔT indicates higher temperature at inner land.

* Assumed to be caused by significant lack of inward flow at inner land.

support external load. Because of the fail safe considerations discussed on page 25 and to enhance proper load distribution, the initial test setup utilized a shim which was ground down to yield a zero fluid film thickness at the 5,000 pound (22,240 Newton) load and zero speed reference.

The results obtained on this setup are summarized in Table 13. This table contains the experimental load versus deflection information as well as additional performance data including flow rates of lubricant, power loss, oil inlet, average film and scavenge temperatures. Fail safe tests were performed at each test point. In order to avoid the possibility of bearing failure at this stage, loading was kept at a level which will yield a minimum film thickness of 1×10^{-3} inches (0.0254 mm) at oil shut-off conditions. Excessive temperature rise caused by a malfunction in the cooling system prevented the running of tests at 20,000 rpm. The highest degree of load sharing was obtained at the 10,000 rpm run where out of a total of 3,560 pounds (15,800 Newtons), 940 pounds (4,200 Newtons) or 26.3 percent of the total externally-applied load was carried by the fluid film bearing. This ratio drops at higher speeds because of the reasons outlined in the previous section.

The power loss of the fluid film bearing at 10,000 rpm runs from 59 percent to 69 percent of the total, depending upon the fluid film bearing clearance. At 15,000 rpm the power loss of the fluid film bearing runs between 63 percent and 76 percent of the total.

In order to permit operation at 20,000 rpm without exceeding the power and cooling capacity of the system, the clearance between the rotor and stator of the fluid film bearing was increased to 1.48×10^{-3} inches (0.038 mm) at the 5,000 pound zero-speed reference point. This brings about a highly unfavorable condition in the load distribution between the fluid film and ball bearing. The test data is summarized in Table 14. As expected from the preliminary analysis, the load carried by the fluid film bearing operating at the new reference condition was practically nil at 20,000 rpm. The total power loss in the test head, because of oil churning, rose to over 60 hp. Since additional power was lost in the spindle, gearbox, and motor, the drive began to go off the line on its overloads when a 62 hp loss in the test head was exceeded. This limited any further exploration at the speed of 20,000 rpm.

To facilitate a direct comparison between the calculated values and actual test data, the load and deflection test data points have been superimposed on the theoretical performance curves previously discussed in Figures 8, 9 and 10. The results shown in Figure 24 indicate very good agreement between the theoretically-predicted and actual test values for both reference settings at 10,000 rpm. The 15,000 rpm test points are compared with the theoretically predicted values in Figure 25. As anticipated from the fluid film bearing test results, the fluid film bearing falls short of carrying its predicted load. At 20,000 rpm test points were obtained only at the 1.48×10^{-3} inch (0.038 mm) setting. The full load as analytically anticipated was carried by the ball bearing; hence, the load versus deflection curve repeats the ball bearing test data shown in Figure 20.

TABLE 13

HYBRID BOOST BEARING PERFORMANCE DATA

(Zero Set-up Clearance at 5000 lb. and Zero Speed)

Rotational Speed rpm	External Load lb. (Newtons)	Fluid Film Thickness 10^{-3} Inch (mm)	Feed Slot Pressure lb/in^2 (10^3 N/m^2)	FF Bearing Load Capacity* lb. (Newtons)	FF Bearing Flow Rate gpm (10^{-4} m^3/sec)	Inlet Oil Temp. ^oF (^oC)	Scavenge Oil Temp. ^oF (^oC)	Average Film Temp. ^oF (^oC)	Radial ΔT ^oF (^oC)	Total Power Loss hp (10^3 watts)
10,000	1000 (4448)	3.95 (0.100)	17.2^S (118.5)	92.2 (410.1)	6.8 (4.29)	206 (96.7)	218 (103.)	221 (105.)	0 (0)	14.4 (10,742.)
	2000 (8896)	2.82 (0.0716)	60.5^S (416.8)	324 (1441.)	6.8 (4.29)	207 (97.2)	223 (106.)	224 (107.)	0 (0)	14.4 (10,742.)
	3000 (13,344)	2.18 (0.0554)	124. ^{S} (854.4)	672 (2989.)	6.8 (4.29)	207 (97.2)	226 (108.)	230 (110.)	0 (0)	16.1 (12,011.)
	3560 (15,834)	1.71 (0.0434)	175. ^{S} (1206.)	940 (4181.)	6.8 (4.29)	208 (97.8)	230 (110.)	231 (110.)	0 (0)	19.1 (14,248.)
15,000	1000 (4448)	5.19 (0.132)	0 (0)	0 (0)	3.7 (2.33)	205 (96.1)	236 (113.)	230 (110.)	0 (0)	11.6 (8650)
	2000 (8896)	3.80 (0.0965)	16.7^S (115.1)	89.5 (389.1)	5.5 (3.47)	211 (99.4)	248 (120.)	248 (120.)	5.12 (2.84)	26.8 (19,993.)
	3000 (13,344)	3.22 (0.0817)	74.5 (513.3)	400 (1779.)	6.3 (3.97)	227 (108.)	275 (135.)	275 (135.)	56.3 (31.2	41.5 (30,959.)
	4000 (17,792)	2.25 (0.0572)	116 (799.2)	620 (2758.)	5.6 (3.53)	251 (122.)	297 (147.)	297 (147.)	10.2 (5.65)	40.7 (30,362.)

Set-up clearance - δ_f = 0 at 5000 lb. (22,240 Newton) axial load; zero rpm

S = Indicates approximate flow rate equilibrium

* Load based on an effective area A_e = 5.36 in^2 (3.4 x 10^{-3} m^2)

TABLE 14

FULL HYBRID BOOST BEARING
PERFORMANCE DATA FAIL SAFE CONFIGURATION

Inlet Oil Temperature
T_o = 200°F

Rotational Speed rpm	External Load lb. (Newtons)	Fluid Film Thickness 10^{-3} in (mm)	Feed Slot Pressure lb/in^2 (10^3 N/m^2)	FF Bearing Load Capacity lb. (Newtons)	FF Bearing Flow Rate gpm (10^{-4} m^3/sec)	Total Power Loss hp (watts)
10,000	1000 (4448)	5.01 (0.127)	1.5 (10.3)	8.0 (35.6)	6.7 (4.23)	12.2 (9101)
	3000 (13,344)	3.32 (0.084)	36.0 (248.)	139 (618.)	6.7 (4.23)	16.9 (12,607.)
	5000 (22,240)	2.28 (0.058)	74.5 (327.)	400 (3,113.)	6.7 (4.23)	17.7 (13,204.)
15,000	1000 (4448)	6.35 (0.161)	0 (0)	0 (0)	4.1 (2.59)	20.9 (15,591.)
	3000 (13,344)	4.10 (0.104)	0 (0)	0 (0)	4.0 (2.52)	21.8 (16,263.)
	5000 (22,240)	2.88 (0.073)	37.5 (258.)	201 (894.)	4.1 (2.59)	29.8 (22,231.)
20,000	1000 (4448)	8.92 (0.226)	0 (0)	0 (0)	4.1 (2.59)	60.9 (45,431.)
	3000 (13,344)	7.27 (0.185)	0 (0)	0 (0)	4.2 (2.64)	54.0 (40,284.)
	5000 (22,240)	5.32 (0.135)	0 (0)	0 (0)	4.3 (2.71)	58.6 (43,716.)

Set-up clearance - δ_f 1.48 x 10^{-3} inch (0.0375 mm) at 5000 lb. (22240 N) axial load, zero rpm.

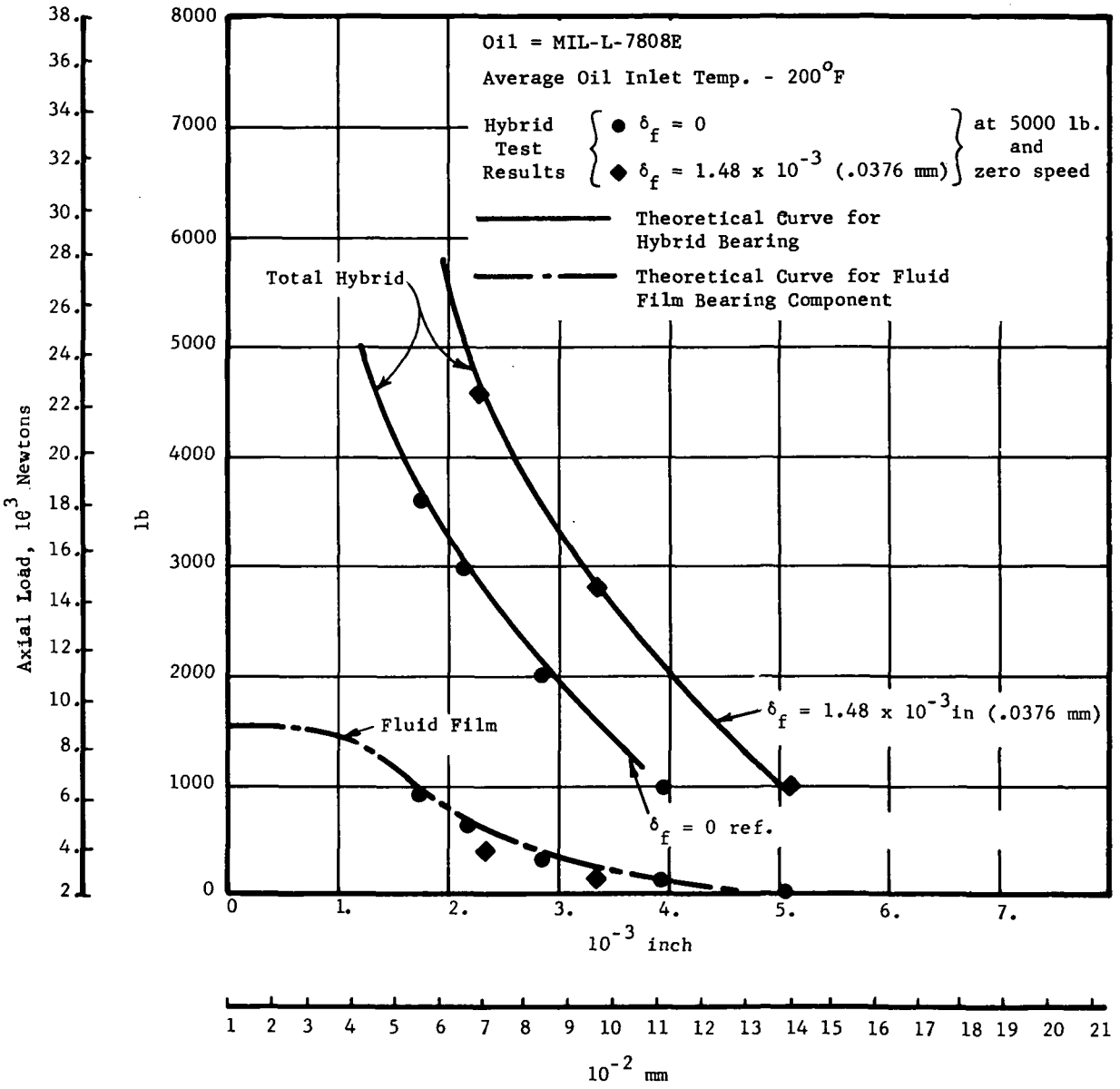

Fig. 24 Performance Characteristics of Total Hybrid Boost Bearing at 10,000 rpm

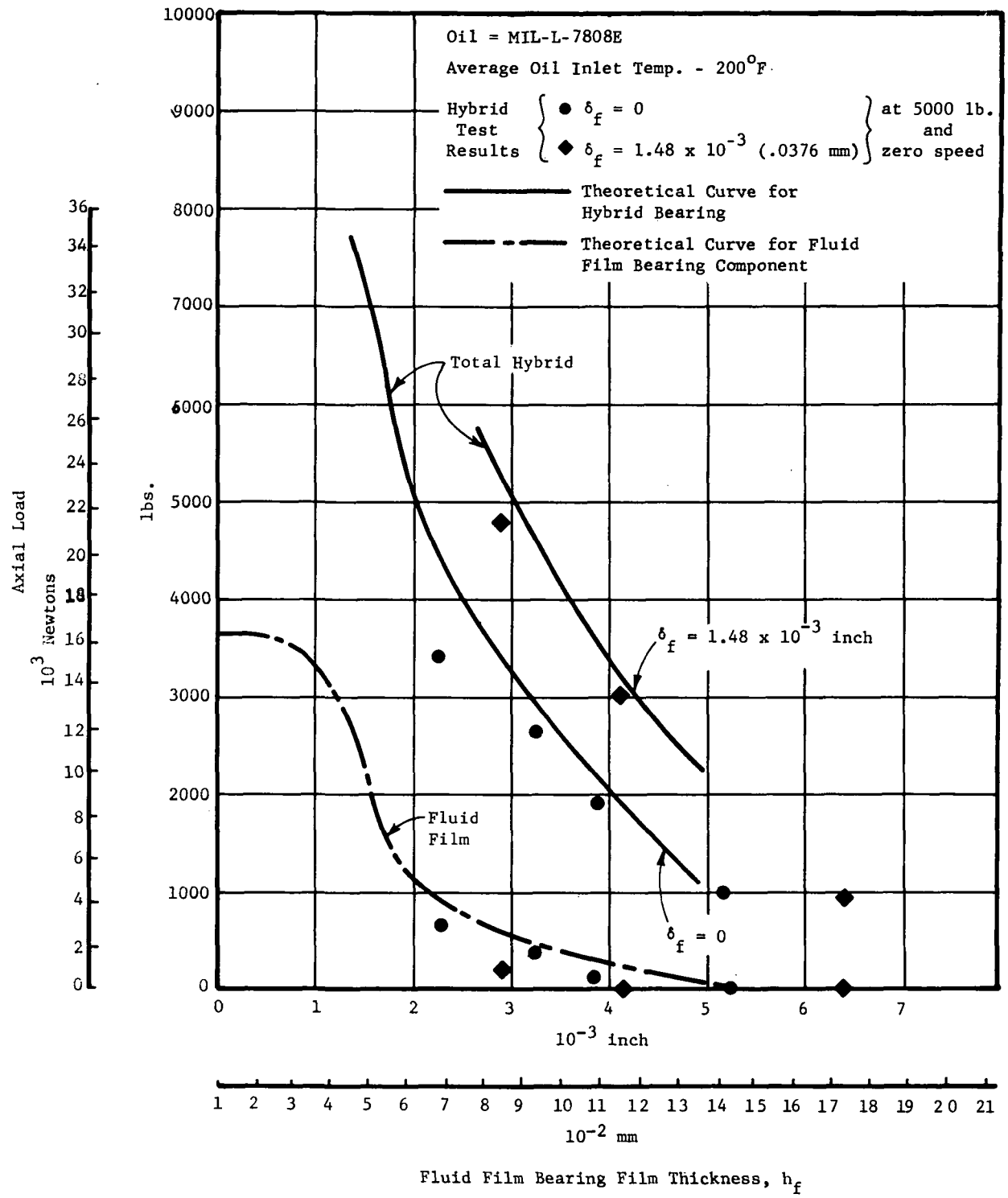

Fig. 25 Performance Characteristics of Hybrid Boost Bearing at 15,000 rpm

REFERENCES

1. Coe, H.H., Scibbe, H.W., Anderson, W.J., "Evaluation of Cylindrically Hollow (Drilled) Balls in Ball Bearings at DN Values to 2.1 Million," Lewis Research Center, Cleveland, Ohio, NASA TN D-7007.

2. Wood, W.W., Ford, R.A., Riza, J.H., "Final Report on Fabrication Development of Hollow Balls," AFML-TR-67-10, W.P.A.F.B., Ohio.

3. Potts, J.R., "Manufacturing Methods for Production of Hollow Ball Bearings for Use in Gas Turbine Engines," Pratt & Whitney Aircraft Division - Fifth Interim Technical Report 1R-121-0(V), July 1971-Sept. 1971. Contract F33615-70-C-1524, MPBMTD, W.P.A.F.B., Ohio.

4. Robinson, J.F., Shackelford, L.A., Joffs, R.E., "The Compliant Ball Bearing" Bearing Conference Proceedings - Thayer School of Engineering-AOA, Dartmouth College, Hanover, N.H., Sept. 1968.

5. Vigh, Zoltan, "Hertz Stress Reduction in Anti Friction Bearings," Bearing Conference Proceedings - Thayer School of Engineering - AOA, Dartmouth College, Hanover, N.H., Sept. 1968.

6. Jones, A.B., "A General Theory for Elastically Constrained Ball and Radial Roller Bearings Under Arbitrary Load and Speed Conditions," ASME Trans., Vol. 82, Series D, No. 2, June 1960, pp. 309-320.

7. The Rolling Element Committee, The Lubrication Division of the ASME, "Life Adjustment Factors for Ball and Roller Bearings," ASME, N.Y., N.Y., Sept. 1971.

8. Wilcock, D.F., Winn, L.W., "The Hybrid Boost Bearing - A Method of Obtaining Long Life in Rolling Contact Bearing Applications," ASME Trans., Vol. 92, Series F, No.3, July, 1970, pp. 406-414.

9. Winn, L.W., "Development and Test of Long Life, Hybrid Boost Thrust Bearings for Small, High Speed Jet Engine Applications," MTI 69TR17, Prepared for Navy under contract No. NOOO19-68-C-0269, June 1969.

10. Winn, L.W. and Badgley, R.H., "Development of Long Life Jet Engine Thrust Bearings, NASA CR-72744, Prepared for NASA Lewis under Contract No. NAS 3-11163, June 1970.

11. Anderson, W.J., Fleming, David P., Parker, Richard J., "The Series Hybrid Bearing - A New High Speed Bearing Concept," ASME Trans., Vol. 94, Series F, No. 2, April 1972, pp. 117-124.

12. Nypan, L.J., Hamrock, B.J., Scibbe, H.W., "Optimization of Conical Hydrostatic Bearing for Minimum Friction," ASME Trans., Vol. 94, Series F, No. 2, April 1972, pp. 136-142.

REFERENCES (Continued)

13. Pan, C.H.T., and Malanoski, S.B., "Analysis of Oil-Lubricated, Fluid-Film, Thrust Bearings with Allowance for Temperature Dependent Viscosity," NASA Report CR-2052, May 1972.

14. "Technical Design Systems Handbook," edited by Dr. H. Rothbart, McGraw-Hill, 1965, Chapter 13 by A.B. Jones.

15. Nemeth, Z.N., Macks, E.F. and Anderson, W.J., "Investigation of 75 mm Bore Deep Grooved Ball Bearing Under Radial Load at High Speeds. II - Oil Inlet Temperature, Viscosity, and Generalized Cooling Correlation," NASA TN 3003, 1952.

16. Holmes, P.W., "Evaluation of Drilled-Ball Bearings at DN Values to Three Million, I - Variable Oil Flow Tests," NASA CR-2004, March 1972.

17. Nemeth, Z.N., Anderson, W.J., "Experiments with Rotating, 10 Inch Diameter Externally Pressurized Air Thrust Bearings" Proceedings of the Gas Bearing Symposium, October 1959, USGPO, 1961, pp. 361-382.

18. Cheng, H.S., Chow, C.Y., and Wilcock, D.F., "Behavior of Hydrostatic and Hydrodynamic Noncontacting Face Seals" Journal of Lubrication Engineering, Transactions of ASME, Vol. 90, April 1968, pp. 510-519.

NOMENCLATURE

A_e	Effective area (fluid film bearing) in^2 (mm^2)
C_d	Coefficient of discharge
D	Effective inner race diameter, inches (mm)
D_w	Ball diameter, inches (mm)
d	Orifice diameter, inches (mm)
f_i	Inner race curvature
f_o	Outer race curvature
HP_t	Power loss in shear, HP
HP_p	Pumping power loss, HP
h_f	Fluid film bearing film thickness, inches (mm)
h_s	Maximum preload spring deflection, inches (mm)
$K_{1,2}$	Constants
K_B	Ball bearing axial stiffness lb/in (Kg/m)
K_e	Effective hybrid bearing axial stiffness, lb/in (Kg/m)
K_f	Fluid film bearing axial stiffness, lb/in (Kg/m)
K_s	Preload spring stiffness, lb/in (kg/m)
m	Oil flow, lb/min (Kg/sec)
N	Speed, rpm
n	Number of orifices
P_d	Diametral play in ball bearing, inches (mm)
P_E	Axial play in ball bearing, inches (mm)
P_s	Pocket pressure, lb/in^2
Q	Oil flow, gpm (m^3/sec)
q	Heat loss, Btu/min (joules/sec)
R_e	Reynolds number
R_i	Inner radius of fluid film bearing, inches (mm)

NOMENCLATURE (Continued)

R_o	Outer radius of fluid film bearing, inches (mm)
ΔR	Difference in inner and outer radii of fluid film bearing, inches (mm)
T_f	Oil film temperature, °F (°C)
T_i	Inlet oil temperature, °F (°C)
T_o	Scavenge temperature, °F (°C)
$T_{\text{outer race}}$	Outer race temperature, °F (°C)
ΔT	Temperature rise in oil, °F (°C)
W	Axial load, lb. (Newtons)
α	Coefficient of thermal expansion, in/in/°F (mm/mm/°F)
β	Contact angle, degrees
δ_B	Ball bearing deflection from zero speed reference, inches (mm)
δ_f	Ball bearing deflection with reference to selected static fluid film bearing clearance conditions, inch (mm)
δ_s	Preload spring deflection, inches (mm)
δ_x	Ball bearing deflection from operational speed reference
μ	Oil viscosity, lb-sec/in^2 (cps)

NASA-Langley, 1973 —— 15 E.-7278

NATIONAL AERONAUTICS AND SPACE ADMINISTRATION
WASHINGTON, D.C. 20546

OFFICIAL BUSINESS
PENALTY FOR PRIVATE USE $300

SPECIAL FOURTH-CLASS RATE
BOOK

POSTAGE AND FEES PAID
NATIONAL AERONAUTICS AND
SPACE ADMINISTRATION
451

U.S.MAIL

POSTMASTER : If Undeliverable (Section 158 Postal Manual) Do Not Return

"The aeronautical and space activities of the United States shall be conducted so as to contribute . . . to the expansion of human knowledge of phenomena in the atmosphere and space. The Administration shall provide for the widest practicable and appropriate dissemination of information concerning its activities and the results thereof."

—NATIONAL AERONAUTICS AND SPACE ACT OF 1958

NASA SCIENTIFIC AND TECHNICAL PUBLICATIONS

TECHNICAL REPORTS: Scientific and technical information considered important, complete, and a lasting contribution to existing knowledge.

TECHNICAL NOTES: Information less broad in scope but nevertheless of importance as a contribution to existing knowledge.

TECHNICAL MEMORANDUMS: Information receiving limited distribution because of preliminary data, security classification, or other reasons. Also includes conference proceedings with either limited or unlimited distribution.

CONTRACTOR REPORTS: Scientific and technical information generated under a NASA contract or grant and considered an important contribution to existing knowledge.

TECHNICAL TRANSLATIONS: Information published in a foreign language considered to merit NASA distribution in English.

SPECIAL PUBLICATIONS: Information derived from or of value to NASA activities. Publications include final reports of major projects, monographs, data compilations, handbooks, sourcebooks, and special bibliographies.

TECHNOLOGY UTILIZATION PUBLICATIONS: Information on technology used by NASA that may be of particular interest in commercial and other non-aerospace applications. Publications include Tech Briefs, Technology Utilization Reports and Technology Surveys.

Details on the availability of these publications may be obtained from:

SCIENTIFIC AND TECHNICAL INFORMATION OFFICE

NATIONAL AERONAUTICS AND SPACE ADMINISTRATION

Washington, D.C. 20546